A&A, 706, A274 (2026)
https://doi.org/10.1051/0004-6361/202556691

Astronomy & Astrophysics

Metal-loaded outflows in sub-Milky Way galaxies in the CIELO simulations

Valentina P. Miranda[1,2,⋆], Patricia B. Tissera[1,2], Emanuel Sillero[1,2], Jenny Gonzalez-Jara[1,2], Lucas Bignone[3], Ignacio Muñoz-Escobar[1,2], Susana Pedrosa[3], and Rosa Domínguez-Tenreiro[4]

[1] Instituto de Astrofísica, Pontificia Universidad Católica de Chile, Av. Vicuña Mackenna 4860, 7820436 Santiago, Chile
[2] Centro de Astro-Ingeniería, Pontificia Universidad Católica de Chile, Av. Vicuña Mackenna 4860, 7820436 Santiago, Chile
[3] Instituto de Astronomía y Física del Espacio, CONICET-UBA, Casilla de Correos 67, Suc. 28, 1428 Buenos Aires, Argentina
[4] Departamento de Física Teórica, Universidad Autónoma de Madrid, E-28049 Cantoblanco, Madrid, Spain

Received 1 August 2025 / Accepted 15 December 2025

ABSTRACT

Context. Supernova (SN) feedback-driven galactic outflows are a key physical process that contributes to the baryon cycle by regulating star formation activity, reducing the amount of metals in low-mass galaxies and enriching the circumgalactic (CGM) and intergalactic media (IGM).

Aims. We aim to understand the chemical loop of sub-Milky Way (MW) galaxies and their nearby regions.

Methods. We studied 15 simulated central sub-MW galaxies ($M_* \leq 10^{10}\mathrm{M}_\odot$) and intermediate-mass galaxies ($M_* \sim 10^{10}$ $\mathrm{M}_\odot$) from the CIELO-P7 high-resolution simulations. We followed the evolution of the progenitor galaxies, their properties, and the characteristics of the outflows within the redshift range $z = [0, 7]$. We used two dynamically motivated outflow definitions, unbound outflows, and expelled mass rates to quantify the impact of SN feedback.

Results. At $z \sim 0$, sub-MW galaxies have a larger fraction of their current oxygen mass in the gas phase but have expelled a greater portion beyond the virial radius, compared to their higher-mass counterparts. Galaxies with $M_* < \sim 10^9$ $\mathrm{M}_\odot$ have 10–40 percent of their total oxygen mass within R_{200} in the CGM and an equivalent to 10–60 percent expelled into the IGM. In contrast, more massive galaxies have most of their oxygen mass locked by the stellar populations. The CGM of low-mass galaxies predominantly contains oxygen low-temperature gas, which acts as a metal reservoir. We find that the outflows are more oxygen-rich for sub-MW galaxies, $Z_{\mathrm{out}}/Z_{\mathrm{ISM}} \sim 1.5$, than for higher-mass galaxies, $Z_{\mathrm{out}}/Z_{\mathrm{ISM}} \leq 0.5$, particularly for $z < 2$. Mass-loading factors of $\eta_{\mathrm{out}} \sim 0$–$6$ are detected, in agreement with observations. While a weak dependence of η on mass and circular velocity is found at $z \sim 0$, a stronger anti-correlation appears for higher redshift.

Conclusions. Our results suggest that sub-MW galaxies may store a significant fraction of metals in their CGM and that the anti-correlation between η and stellar mass (or circular velocity) is stronger at $z \sim 2$, which is likely due to a combination of more intense star formation, a higher merger rate, and shallower potential wells.

Key words. methods: numerical – ISM: jets and outflows – galaxies: abundances – galaxies: evolution

1. Introduction

Galaxy formation and evolution is a complex interplay of physical processes such as the accretion of gas and the interactions and mergers of the central systems with satellites (Somerville & Davé 2015). These processes also regulate the star formation activity, mix the chemical elements in the interstellar medium (ISM), and induce radial migration (e.g. Krumholz et al. 2017). The evolution of stars leads to the synthesis of new chemical elements, which are expelled into the ISM–primarily during the final stages of stellar life–accompanied by significant energy release that can power metal-enriched outflows (e.g. Tinsley 1980; Maiolino & Mannucci 2019). Supernova (SN) feedback-driven outflows are expected to be one of the major drivers of the baryon cycle (Péroux & Howk 2020) by reducing the baryon fraction in low-mass galaxies (Davé 2009) and enriching the circumgalactic (CGM) and intergalactic media (IGM) (Christensen et al. 2018). The impact on low-mass galaxies is thought to be stronger due to their shallower potential wells, which facilitate the ejection of material (Dekel & Silk 1986). Galactic outflows can also shape the mass-metallicity relation (MZR) of galaxies, as they might be able to transport enriched material out of galaxies, particularly in low-mass galaxies (Brooks et al. 2007). Additionally, metal-poor gas inflows are also expected to contribute to the modulation of the global metal content of galaxies and hence their location on the MZR (e.g. De Rossi et al. 2012; Zenocratti et al. 2022; Bassini et al. 2024).

Given the important role that SN feedback plays, studying low-mass galaxies becomes particularly relevant. However, low-mass galaxies are challenging to study because they usually have low surface brightness, which makes them harder to detect (e.g. McQuinn et al. 2019). Therefore, higher-mass galaxies have been more extensively studied. In addition, low-mass galaxies represent a key element in solving cosmological discrepancies in the standard Λ Cold Dark Matter Model (ΛCDM), such as the missing satellites problem or the dark matter distribution in dwarf galaxies (Sales et al. 2022; Kanehisa et al. 2024). Therefore, low-mass galaxies play a very important role in constraining galaxy formation theories and sub-grid physics modelling (Ma et al. 2016; Bullock & Boylan-Kolchin 2017).

A key parameter to study the impact of outflows in galaxies is the mass-loading factor (η), which is defined as the rate

---

[⋆] Corresponding author: `valentina.miranda@uc.cl` at which gas is transported out of the system with respect to the star formation rate (SFR). Observations reported η ranging from ~0.5 to 10 for nearby dwarf galaxies (Martin 1999; McQuinn et al. 2019) and up to ~25–60 for extreme starburst systems (Heckman et al. 2015; Perrotta et al. 2023). High-redshift estimates of main-sequence galaxies obtained with the Atacama Large Millimeter/Submillimeter Array (ALMA; Herrera-Camus et al. 2021; Pizzati et al. 2023; Birkin et al. 2025) and of low-mass galaxies observed with the James Webb Space Telescope (JWST; Carniani et al. 2024) range between $\eta = 0.5$ and 10.

In the Local Universe, observational estimations reported by McQuinn et al. (2019) found only a weak dependency on circular velocity or stellar mass. However, for high redshift galaxies ($z \sim 4$–9) there is evidence of a strong dependency on stellar mass, $\eta \propto M_*^{-0.43}$ and $\eta \propto M_*^{-1.3}$, found by Pizzati et al. (2023) and Carniani et al. (2024), respectively. These dependencies agree with the predictions from the Feedback In Realistic Environments (FIRE) simulations (Muratov et al. 2015; Pandya et al. 2021). Additionally, Murray et al. (2005) found that the momentum injection by supernovae (i.e. momentum-conserving outflows) into the galaxy scaled as $\eta \propto V_c^{-1}$, where V_c is the halo circular velocity, whereas energy-conserving outflows seem to correlate the mass-loading factor as $\eta \propto V_c^{-2}$ (Chevalier & Clegg 1985). At $z \sim 0$, hydrodynamical simulations often estimate $\eta \sim 10$–100 (Vogelsberger et al. 2013; Ford et al. 2014; Christensen et al. 2018; Pandya et al. 2021), which are higher than the observed values, but not so different from the new estimations reported at high redshift. We note that results from numerical simulations depend on the numerical implementation used to model outflows and hence, the analysis and comparison with observations is crucial to set constraints on these models, and to understand the role of and impact played by SN outflows (see also Rosdahl et al. 2017; Kim et al. 2020; Roca-Fàbrega et al. 2021).

The exploration of the chemical abundances of the ISM and the CGM offers the possibility to further understand the role of SN feedback and the baryon-metal cycle (Péroux & Howk 2020). In this context, cosmological simulations of galaxy formation are a powerful tool to investigate the complex interplay between SN feedback and the evolutionary history of galaxies. By tracking the progenitor galaxies and their components, gas and stars, back across cosmic time, simulations enable us to directly study the origin and evolution of outflows, as well as the location of the expelled material.

Simulations generally find that dwarf galaxies are more efficient than Milky Way (MW)–mass galaxies at ejecting metals due to the lower potential well (Scannapieco et al. 2008; Christensen et al. 2016; Muratov et al. 2017; Mina et al. 2021). This is in global agreement with theoretical expectations, which consider the relative importance of the injected SN energy and the binding energy of the system Dekel & Silk (1986). However, there is no clear consensus among different numerical experiments regarding the fraction of metals that remain in the dwarf galaxies and their CGM. For example, the FIRE simulation (Hafen et al. 2019) reported that dwarf galaxies could retain between 30 to 100 percent of their metals within all gas inside the virial radius, R_{200}, and between 10 and 60 percent in their CGM. In contrast, Christensen et al. (2018) reported lower retention rates, estimating 30–60 percent for gas within R_{200}, and 15–25 percent in the CGM. Recently, Piacitelli et al. (2025) studied a larger simulated sample of dwarf galaxies and found that the warm and cold phases retained between 5–10 percent of metals formed by the dwarf galaxies. They also found a weak correlation between galaxy mass and the CGM metal retention factor. These differences between numerical results might be due to the differences in the subgrid physics and, potentially, to the different methods and modelling assumed to measure outflows as mentioned before.

In fact, observationally, outflows are often detected using integrated spectra, such as H_α emission lines as tracers of mass loss in galaxies (e.g. Martin 1999; McQuinn et al. 2019; Carniani et al. 2024). In local starburst galaxies, galactic winds are detected using far-UV absorption lines (Heckman et al. 2015; Chisholm et al. 2017), whereas at higher redshift they are usually detected using rest-frame optical emission lines such as [OII] and [OIII] (Weldon et al. 2024) or in the rest-frame far-infrared using the [CII] emission line (e.g. Ginolfi et al. 2020; Herrera-Camus et al. 2021; Pizzati et al. 2023). Works using simulations generally define outflows as gas particles that have positive radial velocities (see Vogelsberger et al. 2013; Muratov et al. 2017; Bassini et al. 2023), or velocities larger than the Bernoulli velocity (Pandya et al. 2021). Other works tracked gas particles and measured outflows by following the material that moved beyond the virial radius of a galaxy as a function of redshift (Ford et al. 2014; Anglés-Alcázar et al. 2017; Christensen et al. 2018). Hence, while global trends might agree, more specific differences might be due to the actual definition of outflows.

In this paper, our main goal is to analyse the impact of SN feedback on the production of outflows and their effect on metal retention in sub-MW galaxies. In particular, we focus on understanding how oxygen is distributed in the different baryonic components in these galaxies and transported via galactic outflows. For this purpose, we studied 15 central galaxies of the high-resolution simulation of the ChemodynamIcal propertiEs of gaLaxies and the cOsmic web (CIELO) project (Tissera et al. 2025). We followed the evolution of the galaxies across their merger trees. We analysed the oxygen abundances of our galaxies, as well as their history of star formation and triggering of outflows. We explored two dynamically motivated definitions of outflows, one based on the binding energy and the other by tracking particles as they move out of the virial radius (e.g. Anglés-Alcázar et al. 2017).

This paper is organised as follows. In Section 2, we provide a brief description of CIELO simulations, our galaxy sample, and the main methodology. In Section 3 we analyse the selected galaxies and their properties in time, and study the main metallicity relations. In Section 4, we analyse for the oxygen distribution in our simulated galaxies, unbound outflows, inflows, and expelled mass. Section 5 discusses the η factor and its dependency on circular velocity and stellar mass at $z \sim 0$. We also study the evolution of η in Sect. 5.2. Finally, in Sect. 6 we summarise our main results and conclusions.

2. The CIELO simulations and galaxies

In this work, we analyse simulated galaxies from the CIELO project, a suite of zoom-in hydrodynamical cosmological simulations (Tissera et al. 2025). In Section 2.1, we provide a brief summary of the main characteristics of the CIELO simulations. A more detailed description of the initial conditions, subgrid physics, and the main properties of the simulated galaxies can be found in Tissera et al. (2025). The subset of CIELO galaxies[1] selected for the analysis is presented in Section 2.2.

---

[1] This work utilises the CIELO galaxy database reported by Gonzalez-Jara et al. (2025).

2.1. The CIELO simulations

The zoom-in CIELO simulations were performed by using a version of the GADGET-3 (Springel 2005). This version incorporates a multiphase model for the gas component, metal-dependent cooling, a prescription for star formation where stars form in dense, cold gas clumps, and feedback by Type Ia and Type II supernovae (SNe) (Scannapieco et al. 2005, 2006). The CIELO simulations adopt an initial mass function (IMF) by Chabrier (2003), with lower and upper cut-offs of 0.1 $M_\odot$ and 40 $\mathrm{M}_\odot$, respectively. The chemical SN feedback implemented is taken from Mosconi et al. (2001). This model considers 12 chemical isotopes: ^{1}H, ^{4}He, ^{12}C, ^{16}O, ^{24}Mg, ^{28}Si, ^{56}Fe, ^{14}N, ^{20}Ne, ^{32}S, ^{40}Ca, and ^{62}Zn. Primordial abundances are assumed for the initial gas particles: $X_\mathrm{H} = 0.76$, $Y_\mathrm{He} = 0.24$ and $Z = 0$, where Z is the metallicity defined as the fraction of elements heavier than He in the baryonic component.

Type II supernova are assumed to form at the final phase of the evolution of stars more massive than $8\,\mathrm{M}_\odot$, and their lifetimes are estimated following Raiteri et al. (1996). CIELO adopts the SNII yields by Woosley & Weaver (1995). SNIa are assumed to originate from CO white dwarf systems, in which mass transfers from the secondary to the primary start until it outreaches the Chandrasekhar mass. SNIa yields were taken from Iwamoto et al. (1999), and the lifetimes of the progenitors are taken at random within $[0.1, 1]$ Gyr (Scannapieco et al. 2006). This simple model for the lifetime distributions of the progenitors of SNIa reproduces very well with the results provided by the single-degenerated (SD) model as discussed by Jiménez et al. (2015).

The SN feedback model adopted is able to reproduce galactic mass-loaded winds without introducing mass-dependent scaling parameters. It also includes a multiphase model for the ISM that allows the coexistence of the hot, diffuse phase, and the cold, dense gas phase, where star formation takes place (Scannapieco et al. 2006, 2008). The energy injected by both types of SNe is distributed equally between the cold and hot phases. The energy injected into the cold phase is stored in a reservoir until the gas particles accumulate enough energy to change their thermo-dynamical properties and join the hot phase. The energy injected into the hot phase is instantaneously thermalised. The injection into a cold energy reservoir may delay the effective injection of energy when a galaxy is forming stars at a low rate, but during this period, no outflows are expected. When a gas particle is transformed into stars, the existing energy reservoir is injected into the surrounding gas. The thresholds to separate cold and hot phases have been extensively tested by Scannapieco et al. (2005, 2006).

The initial conditions of CIELO are consistent with the ΛCDM cosmological model, with $\Omega_0 = 0.317$, $\Omega_\Lambda = 0.6825$, $\Omega_b = 0.049$, and $h = 0.6711$ (Planck Collaboration XVI 2014). The initial conditions of the CIELO project are zoom-in regions around target galaxies selected from a dark matter only cosmological simulation. The target haloes were chosen to map different density regions, excluding large groups and clusters. In this work, we use the higher resolution CIELO-P7, centred around a target halo of virial mass[2] $M_{200} = 1.3 \times 10^{12}\,\mathrm{M}_\odot$. Tissera et al. (2025) reported that this zoom-in region corresponds to a filamentary structure. The initial mass gas particles have $m_\mathrm{g} = 3.1 \times 10^4\,\mathrm{M}_\odot$ and the dark matter particles have $m_\mathrm{dm} = 2.0 \times 10^5\,\mathrm{M}_\odot$.

CIELO-P7 hosts haloes of virial mass within the range, $M_{200} \sim 10^{10}$–$10^{12}\,\mathrm{M}_\odot$. The virialised haloes were identified using a friends-of-friends algorithm (FoF, Davis et al. 1985), and the substructures within each halo were individualised by using the SUBFIND algorithm (Springel et al. 2001; Dolag et al. 2009). The most massive substructure within a viral halo is classified as a central galaxy. Finally, the merger trees were built using the AMIGA algorithm (Knollmann & Knebe 2009).

2.2. The CIELO-P7 galaxies

We studied 15 central galaxies[3] from CIELO-P7 simulations. We traced the evolution of their progenitor galaxies over 89 snapshots of the simulations, covering the redshift range $z = [0, 7]$. The snapshots have a time separation (Δt) of a median of 1.6×10^8 yr with a minimum and maximum of 5×10^7yr and 1.7×10^8 yr. This time resolution allows us to effectively measure the impact of the SN feedback on the production of outflows, as we define in Sect. 3. We named them according to their SUBFIND IDs at $z = 0$ as shown in Table D.4. These galaxies have stellar masses within the range $10^8 < M_*/\mathrm{M}_\odot < 10^{11}$. Hereafter, we denote those with $M_* < 10^{10}\,\mathrm{M}_\odot$ as sub-MW galaxies.

Galaxies were reoriented by aligning the z-axis with the angular momentum vector of the stellar component of each simulated galaxy in our sample. Within this new system of reference, the decomposition of the stellar particles into halo, bulge, and disc was done following the procedure, dubbed AM-E, described by Tissera et al. (2012). This method is based on combining both the binding energy and angular momentum content of stellar particles to define the components. A detailed description can also be found in Gonzalez-Jara et al. (2025).

To classify the galaxies morphologically, we define the bulge-to-total stellar mass ratio, B/T, where the total mass is equal to the bulge and disc mass. We clarify that the AM-E method does not allow the detection of bars, and if this component exists, it is included as part of the bulge. Hence, the B/T ratio has to be taken as indicative of the global morphology of the galaxies. According to this ratio, most of our galaxies have an important stellar spheroidal component but also show clear rotating gaseous as displayed in Fig. 1.

We confine a galaxy as all gas, stars, and dark matter particles within $1.5R_\mathrm{opt}$, where R_opt is defined as the one that encloses 83 percent of the baryonic mass, and within a height set by the maximum height from the disc plane of the stellar particles belonging to the bulge or disc stellar components, h_max. Hence, the ISM is defined as the gas component contained within a galaxy (i.e. $1.5R_\mathrm{opt}$ and h_max) while the CGM is defined as the gas that is located within the R_{200} and does not belong to the ISM. We classify the gas phase and the stellar components along the main branch of the merger trees of each selected CIELO galaxies from $z = 7$ to $z = 0$.

As examples in Fig. 1 we show the face-on (first row) and edge-on (second row) projections for the gas components of the three selected galaxies adopted: 0181, 2627, and 7805. Each galaxy is shown at key stages in the evolution where we detected outflows with the methods described in Sect. 3 (see Fig. 2). In addition, we show the oxygen abundance maps with streamlines showing the gas velocity direction for the same projections (third and fourth rows, respectively). Galaxies 0181 and

---

[2] The virial mass, M_{200}, is defined as the mass enclosed within a sphere of radius R_{200}, at which the mean mass density reaches 200 times the background density.

[3] We did not consider three out of the 18 galaxies of CIELO-P7 because they do not show strong SF nor any outflow features.

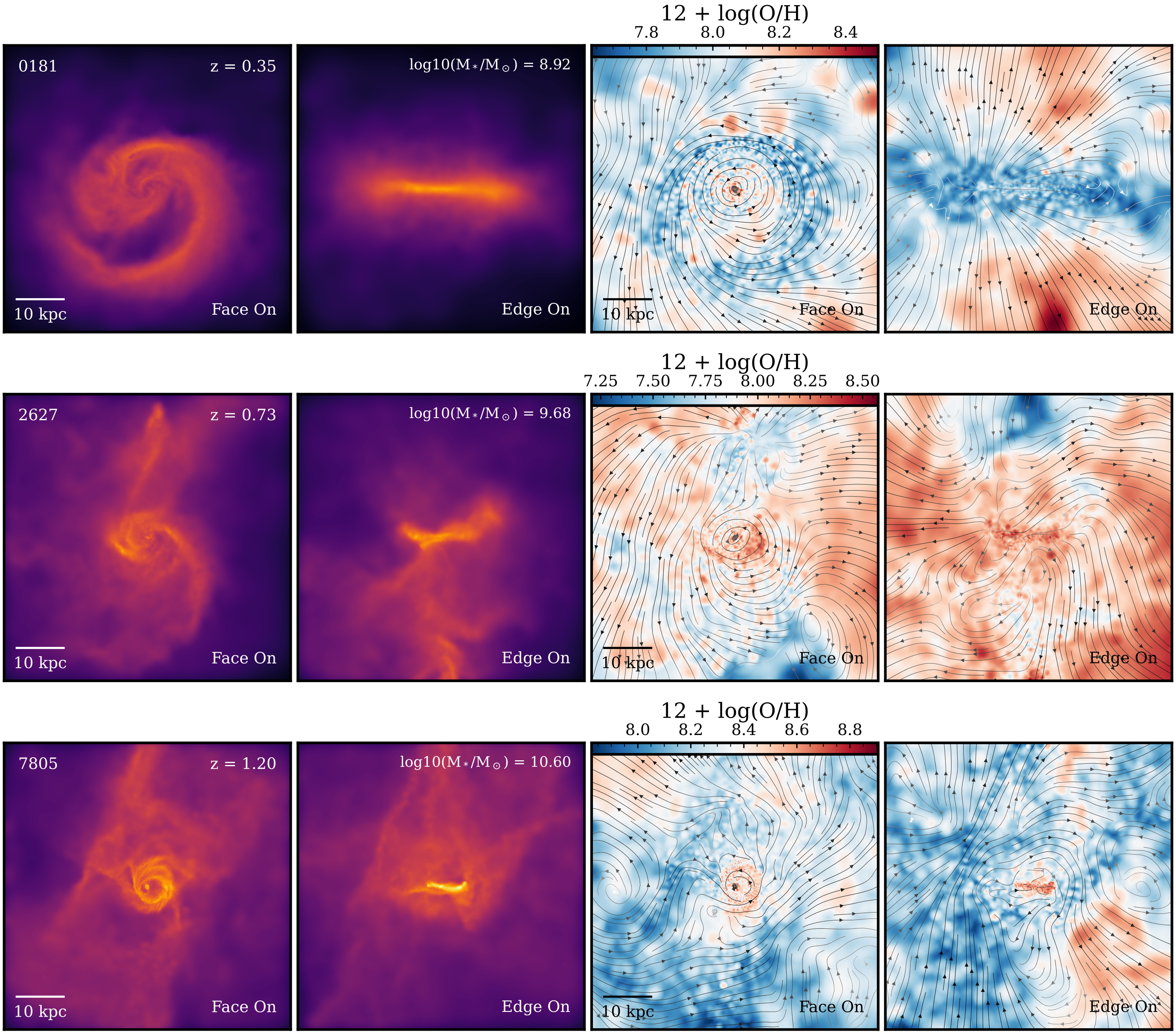

Fig. 1. Face-on and edge-on projected gas density (first two panels, respectively) and the corresponding (O/H) (two right panels) distributions for three selected galaxies of the CIELO-P7 sample: 0181, 2627, and 7805, taken as examples. Each row shows a galaxy at a key stage of its evolution where gas outflows are detected. The M_* of the galaxies at redshift $z = 0$ is shown in each plot. The streamlines depict the median velocity direction of the gas components. The first two galaxies are more rotationally dominated, while the third galaxy has a complex gas structure resulting from a recent gas-rich interaction.

2627 (upper and middle panel) have a well-defined gaseous disc, which exhibits clear signals of gas outflows coming from the central region of the discs and interacting with the CGM (see velocity streamlines). Galaxy 7805, on the other hand, is more massive and has a more dominating stellar spheroidal component. However, as can be seen from this figure, the gas component is also disturbed. We observe that sub-MW galaxies present outflows moving away from the galactic plane in the z-axis. These outflows are oxygen-rich as can be seen in the last two columns of Fig. 1 (face-on and edge-on projections). From this figure, we can see that outflowing material tends to be more enriched or similarly enriched than the ISM. In contrast, higher-mass galaxies such as galaxy 7805 (lower panel) have a less oxygen-rich outflow than the ISM. To understand the nature of these outflows in Section 3, we quantify the level of enrichment in relation to the potential well of the systems to analyse the impact of SN feedback.

3. Outflows, inflows, and star formation rates

In this section, we describe the methods we used to estimate the rate of gas transported in and out of a galaxy and the analysis performed to compare simulations with observations. Regarding the estimation of the outflow rates, there are different approaches in the literature (e.g. Vogelsberger et al. 2013; Muratov et al. 2017; Bassini et al. 2023). In this work, we adopt two dynamically motivated definitions. Our first approach defines unbound outflows by taking into account only the gas moving outwards with enough energy to eventually escape the potential well of its host

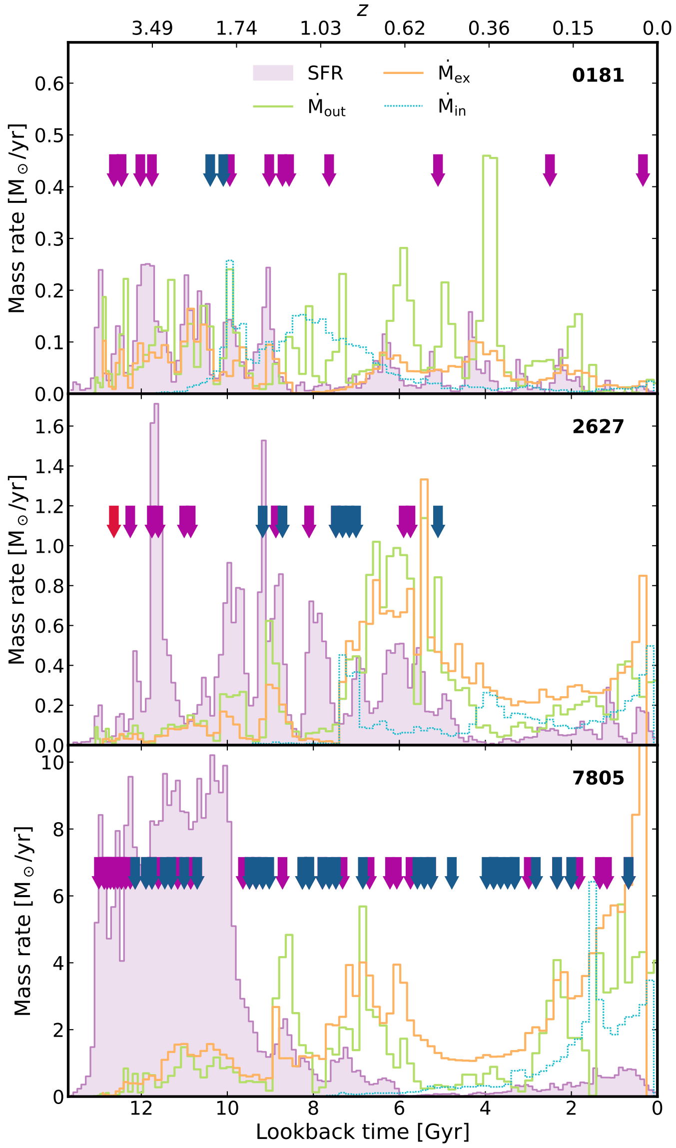

Fig. 2. Three galaxies as examples: evolution of SFR (purple shading), $\dot{M}_{\rm out}$, the rate of unbound outflow for the inner shell $[1.5R_{\rm opt}, 0.5R_{200})$ (solid green lines), $\dot{\rm M}_{\rm ex}$, the expelled mass rates (solid orange lines), and $\dot{M}_{\rm in}$, the inflow mass rate (dotted cyan line) as a function of look-back time (the inset labels denote the galaxy ID). The infall time of satellites (blue arrows) entering the virial radius and the time of minor and major mergers (pink and red arrows, respectively) are also indicated (see Fig. C.1 to see the diversity of behaviour in our sample).

galaxy,

$$\dot{\rm M}_{\rm out}(t) = \frac{\sum_{\rm i} m_{\rm i,out}}{\Delta t}, \tag{1}$$

where the sum is over the i gas particles, which are unbound and are dominated by outward radial motions such that $V_r/\sigma > 1$, with V_r the radial velocity and σ, the velocity dispersion of the gas particles. We estimated these rates within a Δt given by the time interval between two consecutive available snapshots.
The rate $\dot{\rm M}_{\rm out}(t)$ was estimated within two radial bins of the CGM: $[1.5R_{\rm opt}, 0.5R_{200})$ and $[0.5R_{200}, R_{200})$, of a given CIELO galaxy. Hence, for each analysed galaxy, $\dot{\rm M}_{\rm out}(t)$ was estimated in two radial bins and as a function of time.

The second approach adopted is based on the determination of the expelled gas particles. These particles are selected as those that reached galactocentric distances larger than the R_{200} of a galaxy and never re-entered it at subsequent times, i.e. $r > R_{200}$ always remains valid after the particle was expelled the first time. Furthermore, we restrict the gas particles to those with $V_r/\sigma > 0.5$ from $z = 7$ to $z = 0$, so that at high redshift, we only consider the particles with the highest probability of leaving the system. And, for consistency, we maintain this condition down to low values of z. The expelled mass rate is defined as

$$\dot{\rm M}_{\rm ex}(t) = \frac{\sum_{\rm i} m_{\rm i,ex}}{\Delta t}, \tag{2}$$

where the sum is over the mass of gas particles i that, at a given snapshot, do no longer belong to the system, but at the previous snapshot did (i.e. $r_{\rm i} > R_{200}$ with $r_{\rm i}$ being the galactocentric distance of a given particle at a given snapshot). We note that $\dot{M}_{\rm ex}(t)$ could also include material associated with galaxy interactions or splash satellite galaxies. Hence, it is an upper-limit estimation of the action of SN feedback.

We also calculated the rate, η, at which the gas mass is transported out of a system (i.e. $\dot{M}_{\rm ex}(t)$ or $\dot{\rm M}_{\rm out}(t)$), relative to its SFR,

$$\eta = \frac{\dot{\rm M}(t)}{\rm SFR}, \tag{3}$$

where the SFR is defined as $\frac{\sum_{\rm i} m_{\rm i,*}}{\Delta t}$ by considering stellar populations with ages younger than $\Delta t = 0.1\,$Gyr. We study the mass-loading factors and their relation with physical properties in Section 5.

Additionally, we estimate the rate at which the gas that is not associated to the central galaxy at $z = 7$ enters a given galaxy halo at a determined snapshot ($r < R_{200}$), but stays within R_{200} up to $z = 0$. For this purpose, we tracked gas particles in time and calculated the inflow mass rate as

$$\dot{M}_{\rm in}(t) = \frac{\sum_{\rm i} m_{\rm i,in}}{\Delta t}, \tag{4}$$

where the sum is over the mass of gas particles i that, at a given snapshot, is within the R_{200}, but in the previous snapshot was not, $r > R_{200}$.
Finally, we defined the effective inflow mass rate, $\dot{M}^{\rm eff}_{\rm in}$ by applying Eq. (4), but considering only those infalling gas particles that, at a given time, reach the ISM of a galaxy (i.e. $r \leq 1.5R_{\rm opt}$ and $z \leq {\rm h}_{\rm max}$). This rate considers the gas that effectively fell into the ISM of a galaxy and should be considered a lower limit since we do not track the gas particles that fall between snapshots and are transformed into stars.

As an example, in Fig. 2, we display the SFR, the unbound outflows for the first shell $[1.5R_{\rm opt}, 0.5R_{200})$, expelled mass rate, and infall mass rates evolution for a sample of three of our galaxies[4] As can be seen from Table 1, our galaxies have very low star formation activity and some of them are quenched at $z \sim 0$. Only galaxies 2627 and 7805 had recent small starbursts. However, their specific SFR, defined as ${\rm sSFR} = \frac{\rm SFR}{M_*}$, are in good agreement with observations of nearby galaxies of similar mass (Cedrés et al. 2021). In general, all analysed galaxies show bursty star formation histories, albeit with differences in strength and number. We can appreciate this in Fig. 2, where we

---

[4] We show galaxies 0181, 2627, and 7805, just for simplicity as they are good representatives of our sample. A complete picture is shown in Fig. C.1.

Table 1. Main physical properties of the selected CIELO galaxies $z = 0$.

Galaxy ID	$V_{\rm max}$ km s^{-1}	$V_{\rm c}$ km s^{-1}	B/T	$\log(M_{\rm bar}/{\rm M}_\odot)$	$\log(M_*/{\rm M}_\odot)$	sSFR 10^{-11} M$_\odot$ yr^{-1}	12 + log(O/H) dex	$\log(\gamma_{\rm eff})$
2780	35.8	35.8	0.95	8.72	8.04	2.27	7.81	−2.07
2763	39.4	35.1	0.97	8.63	8.12	8.06	8.10	−2.14
2736	24.3	24.3	0.96	8.41	8.17	1.42	8.42	−2.15
9110	31.3	31.3	0.84	8.54	8.26	3.64	8.18	−2.18
2774	42.3	42.3	0.69	8.64	8.40	7.18	8.22	−2.26
0200	12.8	12.8	0.79	8.73	8.68	0.22	8.36	−2.67
0192	55.3	51.3	0.64	9.18	8.81	0.05	8.19	−2.39
0181	70.1	70.3	0.79	9.56	8.92	0.30	8.17	−2.20
2717	68.7	64.7	0.45	9.48	9.11	0.68	8.34	−2.38
2696	75.6	70.7	0.62	9.49	9.38	0.02	8.33	−2.61
2627	94.3	94.3	0.65	9.86	9.68	0.79	8.22	−2.45
0000	102.7	102.7	0.63	9.81	9.73	0.60	8.58	−2.32
8958	111.8	111.8	0.63	10.21	10.17	0.02	8.50	−2.98
7805	152.7	152.7	0.79	10.60	10.60	0.32	8.81	−2.18
2389	218.1	218.1	0.68	10.74	10.72	0.51	8.96	−2.13

Notes. Columns from left to right contain the maximum rotational velocity, the so-called circular velocity as defined in Appendix A, the stellar bulge-to-total ratio, the total baryonic galaxy mass, the total stellar galaxy mass, specific SFR, the oxygen abundance for the star-forming gas, and the effective yields.

show examples of common behaviours. Galaxy 0181 (as well as 2780, 2763, 2736, 9110, 2774, 0200, 2696, 2717, and 2389, shown in Fig. C.1) has several starbursts throughout its evolution. Galaxy 2627 (and 8958, shown in Fig. C.1) has multiple starbursts of comparable strength across time. Galaxy 7805 (as well as 0192 and 0000, shown in Fig. C.1) undergoes a strong and more extended starburst followed by a series of later weaker bursts.

As can be seen from Fig. 2, starbursts are typically followed by a decrease in star formation as the energy released by the SN heats the surrounding gas in conditions of forming stars. The injection of energy can trigger gas outflows of different strengths. In Fig. 2 we also display $\dot{M}_{\rm out}$ and $\dot{M}_{\rm ex}$. As can be seen after the bursts there is often an increase of these rates, indicating the triggering of an unbound outflow and an increment in the expelled mass. In fact, from Fig. 2 it can be appreciated that the peaks of the unbound outflow rates are slightly delayed with respect to the peaks of the SFR comparing with the expelled mass rates[5]. This is due, in part, to the time required for the outflow, produced within the ISM, to reach the CGM. We recall that $\dot{M}_{\rm out}$ is measured in concentric shells as defined in Eq. (1). The peaks of the expelled mass rate agree better in some cases with the starbursts. This can be related to the action of interacting or back-splash galaxies. It has been extensively shown that there is an increase of star formation activity with decreasing pair-wise galaxy separation (e.g. Lambas et al. 2003). This behaviour is reproduced by simulations (e.g. Katz et al. 1999; Tissera et al. 2001; Torrey et al. 2012; Bignone et al. 2019; Rodríguez et al. 2022). These starbursts then induce the SN feedback, driving galactic outflows. In Fig. 2 we also depicted the times of galaxy infall defined when the satellite enters the virial radius of the central galaxies (blue arrows) and the times of mergers, defined as the time when the SUBFIND algorithm no longer recognises the satellites as separate systems for minor mergers (pink arrows) and major mergers (red arrows). We define major mergers as those in which the stellar mass ratio of the satellite galaxy to the central galaxy exceeds $\mu_* = 0.25$ galaxies, and minor mergers as those with $\mu_* < 0.25$. For this analysis we consider satellite galaxies with a baryonic mass larger than 10^6 M$_\odot$ at the time of infall.

In agreement with previous works, we detect that after an interaction or merger with a satellite galaxy, a burst in star formation is often produced, presumably fuelled by the accretion of gas from the satellite. SN events take place soon after the star formation episode, releasing energy into the ISM, which can trigger outflows. However in some cases, the satellite strips gas from the central galaxy during interaction that could be detected as expelled material. An example of this is galaxy 7805, which exhibits an expelled mass rate around 5 Gyr ago, with no SFR counterpart. This is caused by the fact that the expelled mass rate method might include gas particles associated to the tidal stripping of the satellites at larger galactocentric distances. While this caveat adds noise to our estimations, it does not significantly affect our conclusions. In fact, this situation might also be present in observations when galaxies had a close interaction.

It should be noted that each galaxy has a unique formation history shaped by its interactions, mergers, an inflow, and outflow of gas. Therefore, although we summarise the main trends, every system exhibit a distinct evolutionary path, resulting in a diversity of behaviours. This can be seen in more detail in Fig. C.1 for the remaining CIELO-P7 galaxies. Overall, we found that their SFRs are modulated by gas-rich mergers/interactions, as well as the SN feedback-triggered outflows in agreement with previous results.

3.1. *The metallicity of gas outflows and inflows*

During starbursts, gas outflows are expected to transport metals from the galaxy into the CGM (Péroux & Howk 2020). Observational studies support this, finding that the expelled material is enriched with respect to the global ISM (Cameron et al. 2021; Hamel-Bravo et al. 2024; Mishra et al. 2024). In order to study the level of enrichment of the simulation outflows, we estimated the ratio between the metallicity for the unbound outflows within the $[1.5R_{\rm opt}, R_{200})$ shell and the ISM metallicity, $Z_{\rm out}/Z_{\rm ISM}$ at

---

[5] We only show the first shell for simplicity as both shells behave similarly.

each available snapshot[6]. We performed this calculation for each galaxy and its progenitors. To visualise the evolution in time of this ratio and its dependence on stellar mass, in the upper panel of Fig. 3, we show the galaxies coloured by M_* of the central galaxies at $z = 0$. We note that the progenitors have smaller stellar masses, and hence, smaller potential wells, as one moves to higher redshift. We use the stellar mass as a reference to assess the impact of SN feedback to produce chemically enriched outflows with respect to their own ISM or gas inflows.

As can be seen Fig. 3, the outflow metallicity becomes similar to or larger than the ISM metallicity from redshift $z \sim 2$. By this redshift, our simulated galaxies have already had several star formation episodes. At $z > 2$ regardless of the $z = 0$ stellar mass, their lower mass progenitor have outflows which tend to be less enriched than their ISM, except for some systems. We calculated an average of $Z_{\rm out}/Z_{\rm ISM} = 0.56 \pm 0.34$ for the progenitors of massive galaxies, and $Z_{\rm out}/Z_{\rm ISM} = 0.65 \pm 0.61$ for the progenitors of sub-MW galaxies for $z > 2$. For $z \leq 2$ the progenitors of massive galaxies tend to retain more efficiently their metals, with an average of $Z_{\rm out}/Z_{\rm ISM} = 0.39 \pm 0.25$, whereas the progenitors of the sub-MW galaxies have an average of $Z_{\rm out}/Z_{\rm ISM} = 1.13 \pm 0.47$. Outflows are clearly more efficient to transport metals out in sub-MW systems and their progenitors during the whole analysed redshift range. The weaker trend detected at higher redshift could reflect the fact that all progenitors are relatively small systems, similarly susceptible to SN feedback. At lower redshift, the progenitors of massive galaxies become increasingly more massive and therefore less affected by SN feedback, which helps to make the trend more pronounced.

These results are consistent with previous studies from Christensen et al. (2018) where for simulated dwarf and spiral galaxies, an anti-correlation with the stellar mass and a peak in the $Z_{\rm out}/Z_{\rm ISM}$ ratio around $z \sim 2$ were reported. Also, Muratov et al. (2017) found that outflows in lower-mass galaxies ($M_* = 10^7{-}5 \times 10^9$ M$_\odot$) are in general more metal-rich than their ISM where $Z_{\rm out}/Z_{\rm ISM} \sim 1{-}1.5$, similar to what we obtain in this work.

Since metals expelled from a galaxy can later be re-accreted, and gas inflows can penetrate the virial radius (e.g. Ceverino 2017; Collacchioni et al. 2020), we also estimated the ratio between the inflow metallicity and the ISM metallicity. We found that $Z_{\rm in}$ is lower than $Z_{\rm ISM}$ for all analysed galaxies as a function of time. For $z > 2$, we estimated for high-mass systems $Z_{\rm in}/Z_{\rm ISM} = 0.16 \pm 0.19$, whereas for the sub-MW galaxies, an average of $Z_{\rm in}/Z_{\rm ISM} = 0.02 \pm 0.06$. For $z \leq 2$, we found that higher-mass systems have $Z_{\rm in}/Z_{\rm ISM} = 0.15 \pm 0.17$, whereas the sub-MW galaxies, $Z_{\rm in}/Z_{\rm ISM} = 0.18 \pm 0.32$. There is a large scatter in our data, suggesting that the accretion of gas also includes pristine and recycled material from the CGM and IGM. Unlike $Z_{\rm out}/Z_{\rm ISM}$, we find no clear dependence on stellar mass or redshift.

3.2. Mass-metallicity relation

We have already shown that SN feedback can trigger metal-loaded galactic outflows, able to transport material outside of the CIELO galaxies into the CGM and even the IGM. This redistribution of chemical elements can also affect the global metallicity of galaxies and hence, the MZR (Brooks et al. 2007). Therefore, to study the impact of outflows and inflows on the metal content of our galaxies at $z = 0$, we also estimated the MZR (see also Tissera et al. 2025). In Fig. 4, we display the MZR for the star-forming gas (i.e. gas with instantaneous SFR > 0 within the simulated galaxies; purple circles). For comparison, we also calculated the oxygen abundance for the unbound outflows in the first radial bin as previously defined in Section 3 (green circles) and for the expelled mass rates (orange circles). We also include observational and other simulated results[7].

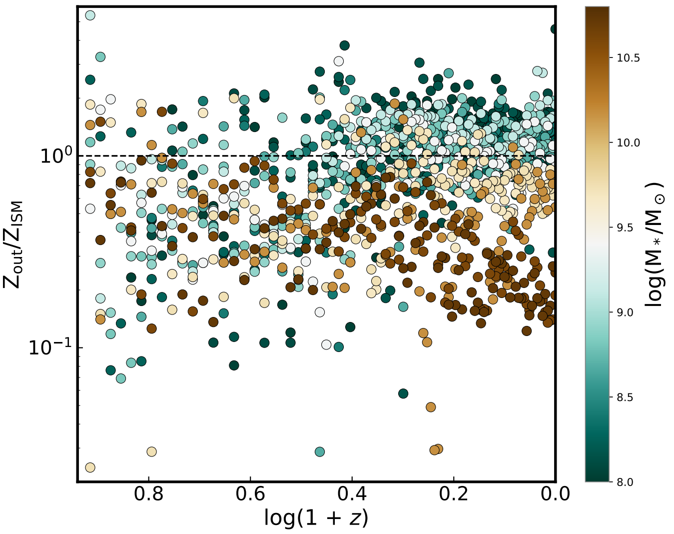

Fig. 3. Ratio of the unbound outflow metallicity to the ISM metallicity, $Z_{\rm out}/Z_{\rm ISM}$, for the analysed galaxy and their progenitors as a function of redshift. The dashed black line shows $Z_{\rm out}/Z_{\rm ISM} = 1$. The colour-code denotes M_* at $z = 0$.

As can be seen from Fig. 4, the SF regions in the analysed galaxies reproduce a MZR in agreement with observations (see also Tissera et al. 2025). The simulated values are within the observed range reported by Lee et al. (2006) with a median scatter of 0.15 dex for the sub-MW galaxies and of 0.12 dex for the higher-mass galaxies with respect to Tremonti et al. (2004) relation. The expelled particles and the unbound outflows determine a weaker relation with stellar mass than the metallicity of the SF gas. For high-mass galaxies, the unbound outflows are less oxygen-rich than the SF regions, while the expelled material has even lower enrichment. However, the level of enrichment of the SF regions and the expelled/outflow material is more similar for sub-MW galaxies[8].

3.3. Effective yields

According to the closed box model Talbot & Arnett (1971), where no inflows or outflows are taken into account, and instantaneous recycling and mixing are assumed, the true stellar yield can be expressed as a function of the gas fraction μ and metallicity Z. Effective yields are obtained based on measured s Z and μ, such that

$$y_{\rm eff} = \frac{Z}{\ln\left(1/\mu\right)}, \tag{5}$$

where Z is defined in Sect. 2 and μ is given by the gas mass in the ISM divided by the total baryonic mass $\mu \approx \frac{M_{\rm g}}{M_* + M_{\rm g}}$. In

---

[6] We note that there are more snapshots covering $z < 1$ as explained in Section 2.

[7] Observations and model by Tremonti et al. (2004) have been rescaled to the adopted solar values $12 + \log({\rm O/H})_\odot = 8.73$ (Lodders 2019) at $M_* = 10^{11}$ M$_\odot$.

[8] It should be noted that Fig. 4 shows the SF gas within the ISM, which only accounts for a part of the total ISM component.

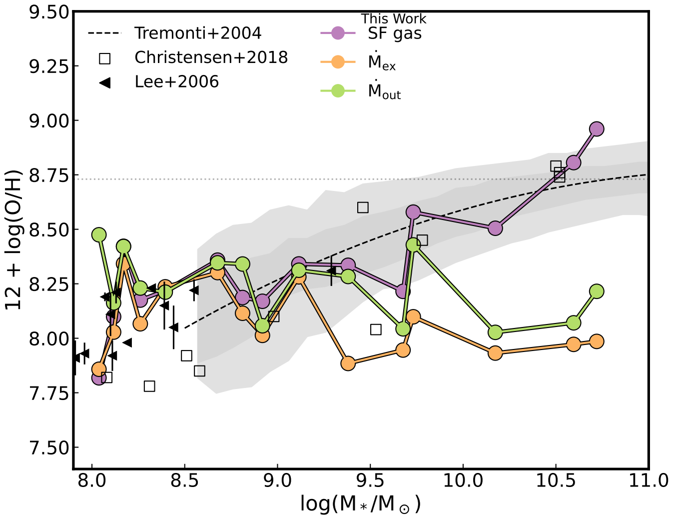

Fig. 4. Mass-metallicity relation for unbound outflows in the first radial interval of the CGM (green circles), for the expelled mass rates (orange circles), and for the star-forming gas (purple circles) for each analysed galaxy. Solid lines are only included to facilitate the visualisation. Observations from Lee et al. (2006, leftwards-pointing triangles) and simulations from Christensen et al. (2018, black squares) are shown. The MZR relation by Tremonti et al. (2004) scaled to solar values of Lodders (2019, dotted line) is shown in dashed black line. The 16-84 percentiles (dark grey contours) and the 2.5–97.5 percentiles (light grey contours) scaled from Tremonti et al. (2004) are also displayed.

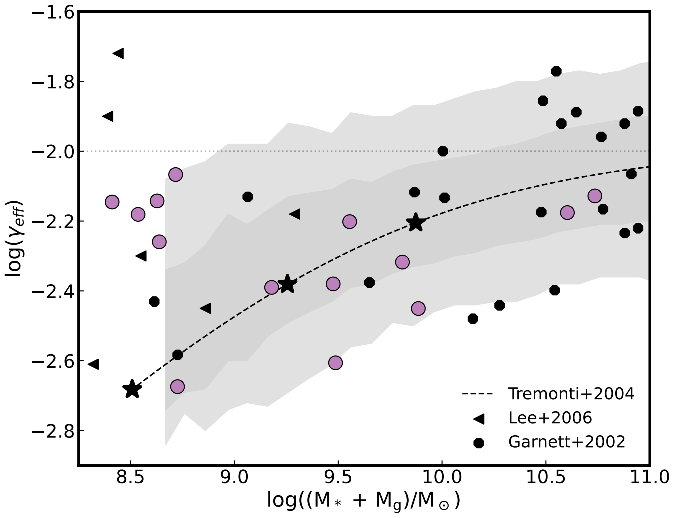

Fig. 5. Effective yields as a function of baryonic mass for our galaxies (purple circles). For comparison, observational results reported by Lee et al. (2006, leftwards-pointing black triangles) and Garnett (2002, black octagons) are also included. The shaded areas denote the 16–84 percentiles (dark grey) and the light grey contour shows the 2.5–97.5 percentiles from observations of Tremonti et al. (2004). Additionally, we show the analytical model fitted by these authors Tremonti et al. (2004, dashed black line). Black stars show the location of systems that have experienced different levels of metal loss: 80, 60, and 40 percent.

a pure closed-box model, a galaxy would tend to have a true yield, γ, independently of the initial gas mass. As a reference, it is usually included the solar value, $\gamma_\odot = 0.01$[9]. The effective yields allow us to estimate how much a galaxy departs from the close box approximation (Dalcanton 2007). In Fig. 5 we show the effective yields estimated for the simulated CIELO galaxies (purple circles) and for observations of nearby dwarf irregular galaxies from Lee et al. (2006) and spiral and irregular galaxies from Garnett (2002).

From Fig. 5 we appreciate that none of our galaxies behaves as perfect closed boxes as expected. However, there is a correlation between $\gamma_{\rm eff}$ and the baryonic mass, where for higher-mass galaxies, the effective yields are larger. This is consistent with sub-MW galaxies experiencing more metal removal from their ISM. The estimated $\gamma_{\rm eff}$ values are given in Table 1. We also incorporated the estimates reported by Tremonti et al. (2004) by employing an analytical model that includes metal ejection by SN outflows. This model was fitted to the observed data, and the star symbols indicate systems with varying degrees of metal loss. Most of our simulated galaxies are consistent with this model, which predicts progressively larger metal losses in lower-mass systems. However, we identify five sub–MW systems in our simulations that do not exhibit the expected level of metal loss but are within the observed range. This can be attributed to their lack of strong starbursts and, consequently, weaker outflows. We note that there are observational data with similar behaviour (Lee et al. 2006). Hence, larger observational and simulated data are needed to better constrain galaxies at the low-mass end, which seem to show a large diversity of behaviours in both simulations and observations (Sales et al. 2022).

As discussed in Section 3.1, inflows are dominated by low-metallicity gas that can dilute the ISM. Hence, we also estimated MZR of the gas inflows to assess the level of enrichment of the accreted gas, finding that the inflows have lower metallicity as shown in Fig. B.1 at $z = 0$. A median of $12 + \log {\rm O/H} = 6.95^{7.28}_{6.16}$ for the sub-MW galaxies and of $12 + \log {\rm O/H} = 7.64^{7.68}_{7.43}$ for the higher-mass galaxies (upper and lower number represent the 75th and 25th percentiles). Outflows tend to be metal-enriched and remove chemical elements from a galaxy. Both processes contribute to lowering the effective yields. As a result, our measurements of the effective yields show some scatter around the observed relation. While the ISM of low-mass galaxies is less-enriched following the MZR, these systems have a significant fraction of gas, producing similar effective yield to massive systems. Overall, we note that there is no clear trend between the effective yields and the total baryonic mass.

4. Mass and oxygen distribution at $z = 0$

In this section, we analyse the distribution of oxygen in the different stellar and gaseous components of our galaxies to assess the metal cycle triggered by SN feedback. In the main panel of Fig. 6 we summarise the oxygen mass distribution per baryonic component for our galaxies. The oxygen mass fractions for each galaxy have been normalised to its total oxygen mass at $z = 0$. Hence, this figure shows the metal budget distribution to the different stellar and gaseous components. Galaxies are ordered according to increasing stellar mass from left to right. For each analysed galaxy, we show the fraction of the oxygen mass in the ISM (purple), the CGM (cyan), and the stellar mass components of the bulge (burgundy), the disc (dark pink), and the stellar halo (light pink). Additionally, the upper panel displays the expelled fraction (orange) defined as the total expelled mass, i.e. the sum of the mass of all expelled gas particles in a range of redshift $z = [0, 7]$, normalised to the total oxygen mass within the virial

---

[9] The solar value was obtained from Tremonti et al. (2004).

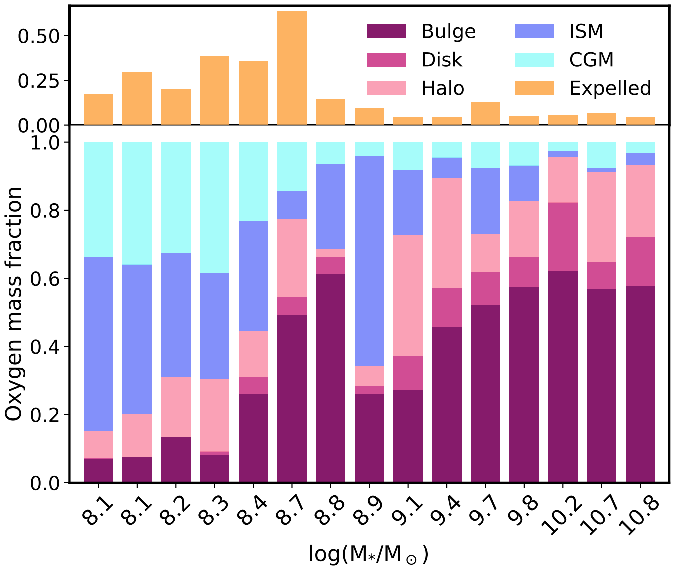

Fig. 6. Lower panel: Oxygen mass fraction for stellar and gas components for our simulated galaxies. Upper panel: Expelled oxygen gas mass fraction to the total oxygen mass in a given galaxy. Galaxies are organised by increasing stellar mass from left to right.

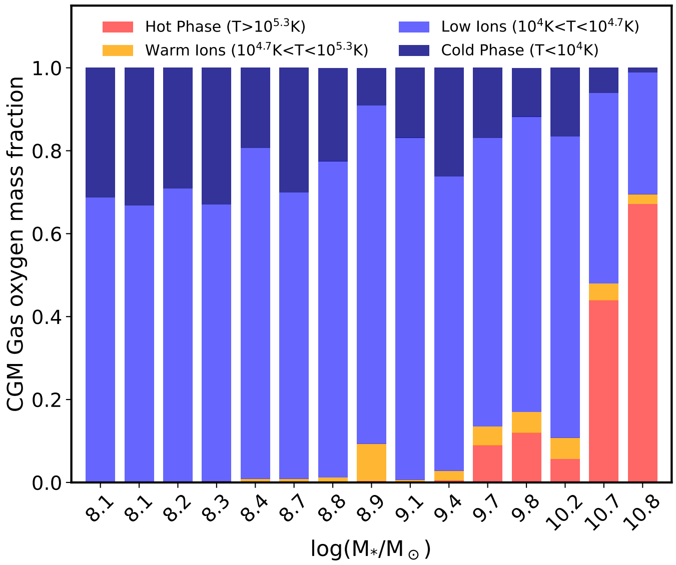

Fig. 7. Oxygen mass fractions in the CGM displayed by gas phase defined according to temperature ranges given by Peeples et al. (2014) and Muratov et al. (2017) (see inset labels). Galaxies are sorted by increasing stellar mass from left to right.

radius at $z = 0$. It provides an estimation of the oxygen mass lost with respect to the current oxygen mass present within R_{200}.

We find that, in high-mass galaxies, the stellar components store about 90 percent of the total oxygen mass. In particular, the bulge of massive galaxies contains a significant amount of oxygen, which decreases rapidly with decreasing stellar mass to account for about 30 percent in the less massive galaxies, $\sim 10^8$ M$_\odot$. Consistently, in these systems the oxygen mass fraction in the ISM and CGM increases. However, there are variations among galaxies of similar masses, which reflect the different evolutionary and star formation histories. We find that, for galaxies with $M_* < 10^{8.7}$ M$_\odot$, the CGM gathers between 10-40 percent of the oxygen found with R_{200}, while for higher mass galaxies, this fraction is less than 10 percent.

As can be seen in the upper panel of Fig. 6, the expelled oxygen mass increases for the decreasing stellar mass galaxies, implying that sub-MW galaxies lose more oxygen than higher-mass systems. Higher-mass galaxies are more efficient at forming stars, locking metals into them. SN driven-outflows are not expected to affect them strongly due to their deeper potential wells and hence, facilitating the retention of metals, as we discuss in the next section. Conversely, lower-mass galaxies have shallower potential wells; therefore, it is easier for the material to escape the galaxy. We estimate that for sub-MW galaxies, an equivalent to ∼10−60 percent of the current oxygen mass was expelled into the IGM, whereas for higher-mass galaxies, this fraction represents less than 10 percent. These estimations agree with previous studies (Muratov et al. 2017; Hafen et al. 2019, see also Sect. 1).

In Fig. 7 we show the breakdown of the oxygen mass stored in the different phases of the CGM. We define different CGM phases according to the gas temperature as hot phase ($T > 10^{5.3}$ K), warm ions ($10^{4.7}$ K $< T < 10^{5.3}$ K), low ions (10^4 K $< T < 10^{4.7}$ K) or cold phase ($T < 10^4$ K), following previous works (Peeples et al. 2014; Muratov et al. 2017; Tumlinson et al. 2017; Roca-Fàbrega et al. 2019). Sub-MW galaxies have a larger fraction of oxygen in low-ion gas phase. Hot phase gas stores a larger fraction of oxygen with increasing stellar mass, as it reaches about ∼70 percent in the CGM of the most massive galaxy in our sample (see Table D.2). On the other hand, the cold phase gas contributes about ∼30 percent of the CGM in sub-MW galaxies, agreeing with Muratov et al. (2017). This is not unexpected since as we move to lower-mass haloes, the virial temperature, $T_{\rm vir}$, also decreases, and the temperature threshold to define the low ions and cold phases are closer to the virial temperature of these small haloes (see Table D.1). Nevertheless, there are variations in the fraction of metals in the hot phase for galaxies with similar masses, which can be attributed to their different evolutionary paths and star formation histories.

5. Mass-loading factors

In this section, we analyse the mass-loading factors, η, and compare them with observations and previous numerical works at $z = 0$, $z = 1$ and $z = 2$. The low number statistics both in simulations and observations prevent us from performing detailed statistical analysis. Instead, we estimated the median values of the CIELO simulated η in the two defined mass intervals: sub-MW and massive galaxies. In the following analysis median η and corresponding 25–75th percentiles are also included.

5.1. Local mass-loading factors

Following Muratov et al. (2017), we computed a redshift-averaged value over $z = [0, 0.5]$ to enable a better comparison with observations[10]. This leads to an artificial high η at $z \sim 0$ (see Eq. (3)) as has also been pointed out in previous works (Pandya et al. 2021). As a result, estimating η from just one snapshot is not feasible. Hence, we obtain the η as defined in Eq. (3) by integrating the SFR and corresponding outflows for $z \leq 0.5$ (5 Gyr). We applied the same definition of Appendix A at all analysed redshifts to estimate $V_{\rm c}$.

---

[10] We note that our sub-MW galaxies, except for galaxy 2627, do not have a recent strong star formation episode.

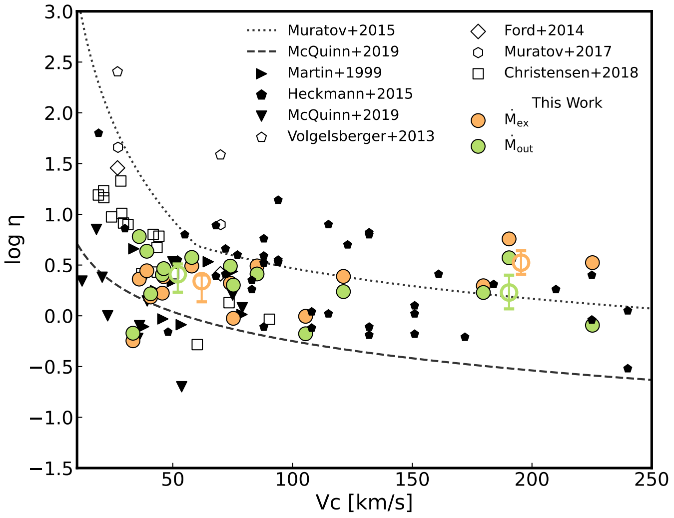

Fig. 8. Mass-loading factors as a function of V_c for CIELO galaxies for $z \leq 0.5$, using the unbound outflow (green circles), and the expelled mass rates (orange circles). Observational data of dwarf, spiral, and starburst galaxies from Martin (1999, rightwards-pointing black filled triangles), and of nearby dwarf galaxies from McQuinn et al. (2019, downwards-pointing black solid triangles) are shown for comparison. Additionally, numerical estimations from Vogelsberger et al. (2013, black open pentagons), Ford et al. (2014, black open diamonds), Muratov et al. (2017, black open hexagons), and Christensen et al. (2018, black open squares). The best fitting regression for the $\eta \propto (1+z)^{1.3} V_c^{-\alpha}$ with $\alpha = 3.2$ for $V_c \leq 60\,\mathrm{km\,s^{-1}}$ and $\alpha = 1$ for $V_c > 60\,\mathrm{km\,s^{-1}}$ at $z = 0.25$ reported by Muratov et al. (2015, black dotted line) and for the $\eta \propto V_c^{-0.96}$ relation reported by McQuinn et al. (2019, dashed black lines) is also depicted. Median values for η_{out} (green open circles) and for η_{ex} (orange open circles) in two mass bins, sub-MW and high-mass galaxies are shown with the corresponding 25–75th percentiles. For visualisation purposes the median values of V_c for the expelled mass rate measurements have been artificially moved +10 km/s.

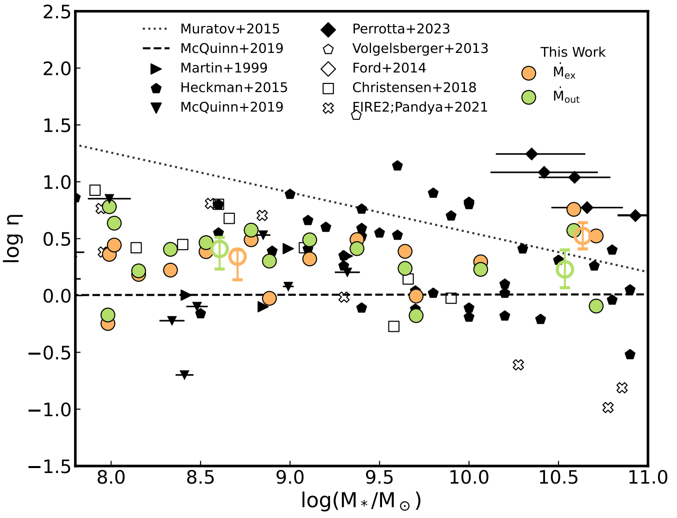

Fig. 9. Mass-loading factors as a function of stellar mass using the unbound outflows and expelled mass rates. The reported relation by Muratov et al. (2015) $\eta \propto M_*^{-0.35}$. Symbols are described in Fig. 8 except for FIRE-2 simulation measurements by Pandya et al. (2021, black cross) and for observational estimations for massive, compact, and starburst galaxies at $z = 0.4$–0.7 by Perrotta et al. (2023, black diamonds). For visualisation purposes the median values of M_* have been artificially moved −0.05 dex for the unbound outflows measurements, and +0.05 dex for the expelled mass rate.

In Fig. 8 we display η as a function of V_c, for the unbound outflows (η_{out}) measured in the first radial bin of CGM and for the expelled mass rate (η_{ex}). Estimations for a variety of simulations and observations are also displayed for comparison.

Our mass-loading factor estimations range between $\eta_{\mathrm{out}} \sim 0.7-6$ for the unbound outflows as shown in Fig. 8 (green circles). The specific values are displayed in Table D.3. This is consistent with observational estimations reported for dwarf galaxies by McQuinn et al. (2019). To quantify a potential trend, we estimated the median values of η_{out} and η_{ex}. We find that sub-MW galaxies have a median of $\log_{10}(\eta_{\mathrm{ex}}) = 0.34^{0.40}_{0.14}$ dex for the expelled mass rate and of $\log_{10}(\eta_{\mathrm{out}}) = 0.41^{0.51}_{0.23}$ dex for the unbound outflows, whereas for high-mass galaxies the median value for the mass-loading factors for the expelled mass rate is $\log_{10}(\eta_{\mathrm{ex}}) = 0.52^{0.64}_{0.41}$ dex and of $\log_{10}(\eta_{\mathrm{out}}) = 0.23^{0.40}_{0.07}$ dex for the unbound outflows.

The CIELO galaxies follow the general observational trend, whereby higher circular velocities correspond to lower mass-loading factors, although the correlation is weaker. Indeed, a Spearman correlation analysis shows that the simulated relations do not seem to depend on V_c as can be seen from Table D.4. Nevertheless, in this table we provide the best-fitting parameters that yield $\alpha \sim 0.3$, consistent with observational results by McQuinn et al. (2019). It should be noted that observations for our mass range also appear to have a weak correlation, whereas for lower masses the dependence on V_c seems to be stronger. As seen in Fig. 8, for the expelled mass rates (orange circles) we obtain slightly higher values, $\eta_{\mathrm{ex}} \sim 0.6$–$5.7$ (e.g. Förster Schreiber et al. 2019; McQuinn et al. 2019; Concas et al. 2022), but consistent with estimated mass-loading factors reported by other numerical works (e.g. Ford et al. 2014; Christensen et al. 2018).

In Fig. 9 we present the mass-loading factors as a function of stellar mass. We show the same observations and simulations for comparison previously mentioned in Sect. 5.1, along with the FIRE-2 simulations by Pandya et al. (2021) and observational data of massive, compact, and starburst galaxies at $z = 0.4$–0.7 from Perrotta et al. (2023). The best fitting relations, $\eta \propto M_*^{0.04}$ from McQuinn et al. (2019), and $\eta \propto M_*^{-0.35}$ from Muratov et al. (2015, FIRE-1) are also shown.

As can be seen from Fig. 9, the simulated η obtained for the CIELO galaxies agree with observations. We note that some numerical simulations reported a stronger correlation with stellar mass (Vogelsberger et al. 2013; Ford et al. 2014), and some of them show mass-loading factors between one and two orders of magnitude higher than observations for low velocity systems, except for FIRE-2 measurements by Pandya et al. (2021). McQuinn et al. (2019) found a very weak negative correlation with stellar mass. As can be seen from Table D.4, we find no significant correlation.

5.2. *Mass-loading factor for $z > 0$*

To study how outflows impact galaxies at different redshift, we study the evolution of the mass-loading factor with redshift. We consider two redshift intervals of $z = 0.5-1.5$ ($z \sim 1$) and $z = 1.5-2.5$ ($z \sim 2$). These redshift intervals provide us information on a particular interesting period of galaxy formation, from the cosmic noon when star formation is more active and hence, the impact of SN feedback is more significant. We followed the same procedure applied for the estimation of the η at $z \sim 0$.

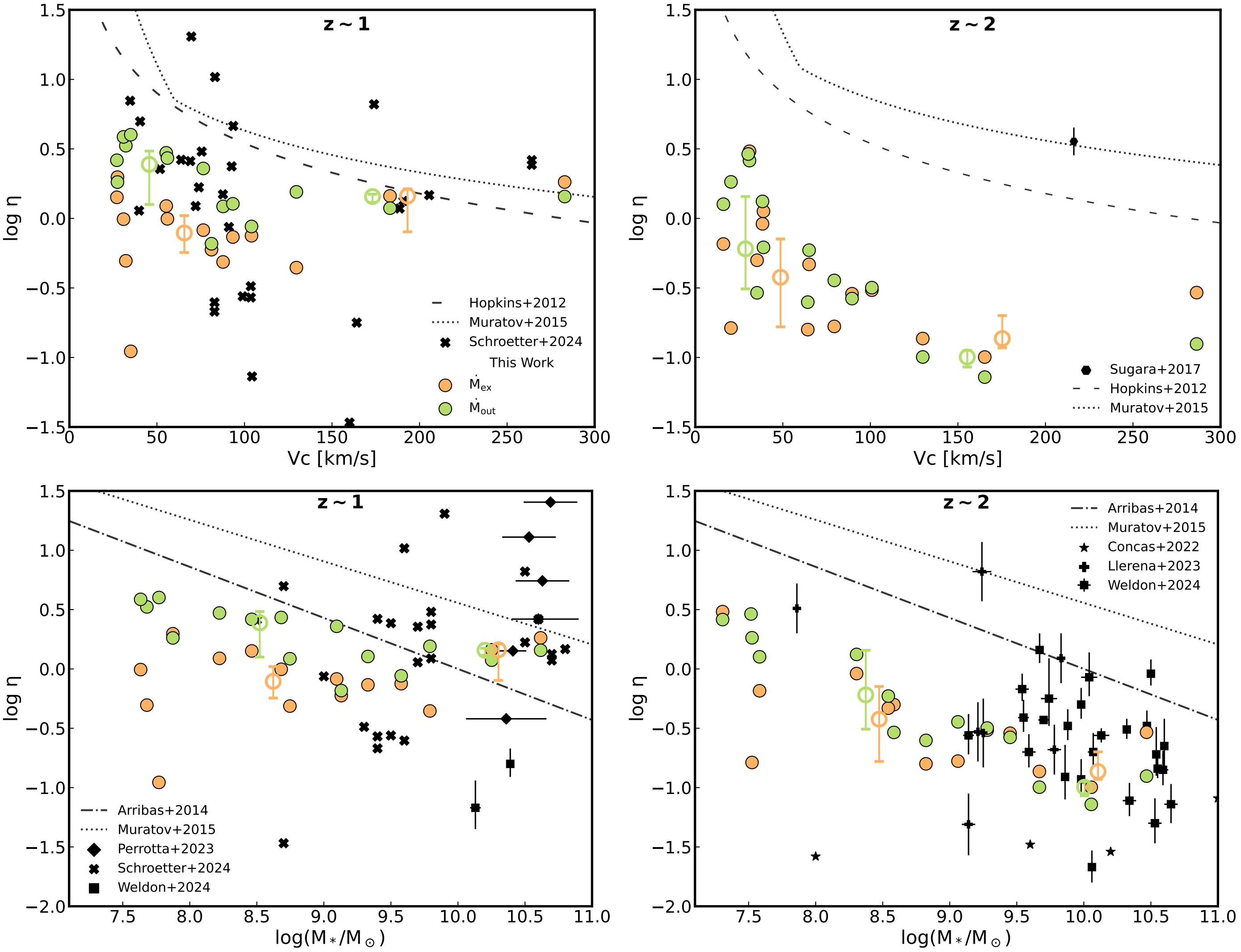

Fig. 10. Mass-loading factor, η, as a function of circular velocity, V_c (upper-panel) and stellar mass, M_* (bottom-panel). Symbols and solid lines for this work and Perrotta et al. (2023) are previously described in Fig. 8. Observational data of star-forming galaxies from MEGAFLOW survey (Schroetter et al. 2016) by Schroetter et al. (2024, black cross) and of star-forming galaxies from the MOSFIRE survey by Weldon et al. (2024, black squares) are shown, both at $z \sim 1$. Observations at $z \sim 2$ of a star-forming galaxy from Sugahara et al. (2017, black hexagon), of main-sequence galaxies from the KLEVER survey by Concas et al. (2022, black stars) and low-mass star-forming galaxies by Llerena et al. (2023, black cross) are also displayed. The best-fitting regression reported by Muratov et al. (2015) previously described in Fig. 9, $\eta \propto V_c^{-1.2}$ for the relation reported by Hopkins et al. (2012, black dashed line) for $z \sim 1$ and $\eta \propto M_*^{-0.43}$ by Arribas et al. (2014, dashed dotted lines) is shown. Median of $\log_{10}(M_*)$ are artificially displayed by +0.05 dex for the expelled mass rate and −0.05 dex for the unbound outflows, and the median of V_c is artificially moved +10 km/s for the expelled mass rate (orange circles) and −10 km/s for the unbound outflows (green circles), for visualisation purposes only.

We also added the median simulated η in each figure. It is important to note that the comparison can only be done in a general way due to the low statistical number of data in both observations and simulations. In Fig. 10 we show the mass-loading factor as a function of V_c (upper panels) and M_* (bottom panels) at $z \sim 1$ (left panels) and $z \sim 2$ (right panels). Observations from different authors have been included for comparison, as well as proposed fitting relations.

Our estimations yield $\eta_{\rm out} \sim 0.6$–4 for the unbound outflows and $\eta_{\rm ex} \sim 0.1$–2 for the expelled mass as displayed in Fig. 10 (see also Table D.3). For $z \sim 1$, sub-MW galaxies have a median of $\log_{10}(\eta_{\rm ex}) = -0.10^{0.02}_{-0.24}$ dex for the expelled mass rate and of $\log_{10}(\eta_{\rm out}) = 0.38^{0.48}_{0.10}$ dex for the unbound outflows, whereas for higher-mass galaxies the median value for the mass-loading factors for the expelled mass rate is $\log_{10}(\eta_{\rm ex}) = 0.16^{0.21}_{-0.10}$ dex and of $\log_{10}(\eta_{\rm out}) = 0.16^{0.17}_{0.12}$ dex for the unbound outflows.

For the expelled mass the trends are very weak, and we find no significant correlation. The $\eta_{\rm out}$ obtained for the analysed CIELO galaxies are consistent with available observations of Schroetter et al. (2024) at $z \sim 1$ with $\eta^a_{\rm out} \propto V_c^{-0.48}$ for the unbound outflows. This correlation seems to be stronger at $z \sim 2$ (upper-right panel), which yields $\eta^a_{\rm out} \propto V_c^{-0.77}$ and of $\eta_{\rm ex} \propto V_c^{-0.38}$ for the expelled mass (see Table D.4 for the Spearman correlation factors). Our fitted relations follow the observational data, suggesting that sub-MW galaxies are more affected by SN outflows than high-mass galaxies as expected.

Finally, in Fig. 10 (bottom panel), we study the dependence on M_*. At $z \sim 1$ we obtain a weak dependence on stellar mass at redshift (bottom left panel) of $\eta^a_{\rm out} \propto M_*^{-0.21}$, but statistically significant as can be seen from Table D.4. The trends are consistent with observed galaxies (Perrotta et al. 2023; Schroetter et al. 2024; Weldon et al. 2024). Similarly to the trend with V_c, we find that the dependence on M_* is stronger at $z \sim 2$, which yields $\eta^a_{\rm out} \propto M_*^{-0.30}$ and of $\eta_{\rm ex} \propto M_*^{-0.37}$ (see also Table D.4). Our estimates agree with observations at the high-mass end (Concas et al. 2022; Llerena et al. 2023; Weldon et al. 2024). However, there are very limited observations for dwarf galaxies at this redshift. For $z \sim 2$, sub-MW galaxies have a median of $\log_{10}(\eta_{\rm ex}) = -0.42^{-0.15}_{-0.78}$ dex for the expelled mass rate and of $\log_{10}(\eta_{\rm out}) = -0.22^{0.16}_{-0.51}$ dex for the unbound outflows, whereas for higher-mass galaxies the median value for the mass-loading factors for the expelled mass rate is $\log_{10}(\eta_{\rm ex}) = -0.86^{-0.68}_{-0.93}$ dex and of $\log_{10}(\eta_{\rm ex}) = -1.00^{-0.95}_{-1.07}$ dex for the unbound outflows. For these figures, the median of $\log_{10}(M_*)$ has been artificially displayed by +0.05 dex for the expelled mass rate and −0.05 dex for the unbound outflows, and the median of V_c is artificially moved +10 km/s for the expelled mass rate (orange circles) and −10 km/s for the unbound outflows (green circles), for visualisation purposes only.

In summary, we observe that the mass-loading factor shows a clearer anti-correlation with V_c and M_* for higher redshift. This dependence is consistent with the fact that the SFR increases with redshift and galaxies became smaller and hence, more susceptible to being affected by SN feedback. As shown in Fig. C.1, the frequency of mergers increases with redshift and their occurrences are also associated to the occurrences of starbursts, indicating a connection between them as suggested by observational and simulated works (e.g. Tissera et al. 2001; Kohandel et al. 2025). As mentioned, the progenitors are also lower mass systems which makes them easier to trigger galactic outflows. We speculate these are the reasons behind the stronger correlations. As we move to lower redshift, the star formation diminishes and there are no clear correlations with mass or velocity at least for the CIELO galaxies.

6. Conclusions

We studied 15 central galaxies of the high-resolution CIELO-P7 cosmological simulations (Tissera et al. 2025), focussing on the sub-MW galaxies ($M_* < 10^{10}\,{\rm M}_\odot$). We followed the progenitor galaxies between redshift $z = [0, 7]$ and measured unbound outflows in two shells of the CGM $[1.5R_{\rm opt}, 0.5R_{200}]$ and $[0.5R_{200}, R_{200})$, and expelled mass rates ($r > R_{200}$). We applied these two dynamically motivated definitions of outflows. We summarise our main results as follows:

1. We find that minor and major mergers and interactions, as well as SN feedback triggered by these events, can modulate the SFR histories of sub-MW galaxies. A tidally induced or merger-induced burst of SF triggers mass-loaded outflows, which decreases the star formation activity, as expected, due to the energy release of SN into the ISM, and transports enriched material out of a galaxy. However, we note that the impact of mergers on star formation and the galactic outflow is complicated and might depend on other parameters such as the gas-richness and the orbital characteristics of the encounters. A detailed analysis of these aspects is beyond the scope of this paper.
2. The outflow metallicity becomes significant relative to the ISM metallicity from $z \sim 2$, as many SF episodes have time to enrich a galaxy. For $z > 2$, we estimate a median $Z_{\rm out}/Z_{\rm ISM} \sim 1.5$ for the sub-MW galaxies and a median $Z_{\rm out}/Z_{ISM} \leq 0.5$ for higher-mass galaxies, in agreement with previous studies (e.g. Muratov et al. 2017; Christensen et al. 2018). At higher redshift ($z > 2$), the progenitors of the more massive systems have an average $Z_{\rm out}/Z_{\rm ISM} = 0.56$, while the sub-Milky-Way systems show a higher average ratio of $Z_{\rm out}/Z_{\rm ISM} = 0.67$. Sub-MW galaxies are more efficient in removing metals from their ISM than more massive systems across all redshift.
3. The MZR of our sample is in agreement with observations. The effective yields show a large diversity in agreement with observations, particularly for sub-MW systems. There is a global agreement with predictions from analytical models that allow mass loss. Galaxies also have accreted gas that tends to have a lower metallicity than the star-forming ISM, particularly for sub-MW systems, although there is a large variation. The relative impact of inflows and outflows remains to be analysed.
4. Sub-MW galaxies have a higher fraction of their current total oxygen mass in the gas phase (i.e. ISM or CGM) and have higher fractions of expelled mass at $z = 0$ than higher-mass galaxies. This implies that sub-MW galaxies are more affected by outflows. We find that in galaxies with $M_* < 10^{8.7}\,{\rm M}_\odot$, the CGM contains between 10 and 40 percent of the oxygen mass within R_{200}, whereas in more massive galaxies, this fraction drops below 10 percent. For sub-MW-mass galaxies, an equivalent to approximately 10−60 percent of the present-day oxygen mass has been expelled into the IGM, while in more massive galaxies, this fraction is less than 10 percent. In addition, most of the oxygen in the CGM is in the form of low ion gas for $M_* < 10^{8.7}\,{\rm M}_\odot$. This component seems to be a metal reservoir in the CGM of these galaxies.
5. We obtain a mass-loading factor between $\eta_{\rm out} \sim 0.7$–6 for the unbound outflows and $\eta_{\rm ex} \sim 0.6$−5.7 for the expelled mass rate for $z \leq 0.5$. This is consistent with observations of local dwarf galaxies (McQuinn et al. 2019) and field galaxies (Förster Schreiber et al. 2019). We find no clear signals of correlation between the mass-loading factor and the circular velocity in this redshift range.
6. At $z \sim 1$ we obtain mass-loading factors within the range $\eta_{\rm out} \sim 0.6$–4 for the unbound outflows and $\eta_{\rm ex} \sim 0$−2 for the expelled mass rate, and for $z \sim 2$ between $\eta_{\rm out,ex} \sim 0$−3 for the unbound outflows and for the expelled mass rate. The negative correlation is stronger at higher redshift ($z \sim 2$) with a linear fit $\eta_{\rm out} \sim V_c^{-0.71}$. This suggests that the progenitors of sub-MW galaxies are more affected by SN outflows than those of higher-mass galaxies. The negative correlation is stronger at $z \sim 2$ as progenitors of the selected galaxies are more actively forming stars, have more frequent minor and major mergers, and lower potential wells.

The CIELO galaxies are able to reproduce global observed trends of sub-MW galaxies and provide a reference to compare with observations and with simulations using different subgrid physics. Sub-MW galaxies provide important constraints to test subgrid modelling. We predict that a significant fraction of metals in low-mass galaxies are stored in the cool components of their CGM. Due to the high number abundance of dwarf galaxies, they could represent a significant reservoir of chemical elements.

Acknowledgements. We thank the anonymous referee for their rigorous and insightful comments which helped improve the clarity of this manuscript. We gratefully thank the EvolGal4D team for the insightful discussions throughout this work. We also thank Brian Tapia-Contreras for developing the code used to produce Fig.1. VPM acknowledges funding by ANID (Beca Magíster

Nacional, Folio 22241063). PBT acknowledges partial funding by Fondecyt-ANID 1240465/2024. JGJ acknowledges funding by ANID (Beca Doctorado Nacional, Folio 21210846). ES thanks partial financial support by Fondecyt-ANID Postdoctoral 2024 Project N°3240644. RDT thanks the Ministerio de Ciencia e Innovación (Spain) for financial support under Project grant PID2021-PID2024-156100NB-C21 financed by MICIU/AEI /10.13039/501100011033 / FEDER, EU. We acknowledge ANID Basal Project FB210003 and Núcleo Milenio ERIS. This work has received financial support from the European Union's HORIZON-MSCA-2021-SE-01 Research and Innovation programme under the Marie Sklodowska-Curie grant agreement number 101086388 – Project acronym: LACEGAL. This project used the Ladgerda Cluster (Fondecyt 1200703/2020 hosted at the Institute for Astrophysics, Chile), the NLHPC (Centro de Modelamiento Matemático, Chile) and the Barcelona Supercomputer Center (Spain). This work made use of Astropy (Astropy Collaboration 2013) and Py-SPHViewer (Benitez-Llambay 2015), we acknowledge the developers.

References

Anglés-Alcázar, D., Faucher-Giguère, C.-A., Kereš, D., et al. 2017, MNRAS, 470, 4698
Arribas, S., Colina, L., Bellocchi, E., Maiolino, R., & Villar-Martín, M. 2014, A&A, 568, A14
Astropy Collaboration (Robitaille, T. P., et al.) 2013, A&A, 558, A33
Bassini, L., Feldmann, R., Gensior, J., et al. 2023, MNRAS, 525, 5388
Bassini, L., Feldmann, R., Gensior, J., et al. 2024, MNRAS, 532, L14
Benitez-Llambay, A. 2015, py-sphviewer: Py-SPHViewer v1.0.0
Bignone, L. A., Helmi, A., & Tissera, P. B. 2019, ApJ, 883, L5
Birkin, J. E., Spilker, J. S., Herrera-Camus, R., et al. 2025, ApJ, 985, 243
Brooks, A. M., Governato, F., Booth, C. M., et al. 2007, ApJ, 655, L17
Bullock, J. S., & Boylan-Kolchin, M. 2017, ARA&A, 55, 343
Cameron, A. J., Fisher, D. B., McPherson, D., et al. 2021, ApJ, 918, L16
Carniani, S., Venturi, G., Parlanti, E., et al. 2024, A&A, 685, A99
Cedrés, B., Pérez-García, A. M., Pérez-Martínez, R., et al. 2021, ApJ, 915, L17
Ceverino, D. 2017, in The Galaxy Ecosystem. Flow of Baryons through Galaxies, 7
Chabrier, G. 2003, ApJ, 586, L133
Chevalier, R. A., & Clegg, A. W. 1985, Nature, 317, 44
Chisholm, J., Tremonti, C. A., Leitherer, C., & Chen, Y. 2017, MNRAS, 469, 4831
Christensen, C. R., Davé, R., Governato, F., et al. 2016, ApJ, 824, 57
Christensen, C. R., Davé, R., Brooks, A., Quinn, T., & Shen, S. 2018, ApJ, 867, 142
Collacchioni, F., Lagos, C. D. P., Mitchell, P. D., et al. 2020, MNRAS, 495, 2827
Concas, A., Maiolino, R., Curti, M., et al. 2022, MNRAS, 513, 2535
Dalcanton, J. J. 2007, ApJ, 658, 941
Davé, R. 2009, in Galaxy Evolution: Emerging Insights and Future Challenges, eds. S. Jogee, I. Marinova, L. Hao, & G. A. Blanc, ASP Conf. Ser., 419, 347
Davis, M., Efstathiou, G., Frenk, C. S., & White, S. D. M. 1985, ApJ, 292, 371
De Rossi, M. E., Tissera, P. B., & Pedrosa, S. E. 2012, A&A, 546, A52
Dekel, A., & Silk, J. 1986, ApJ, 303, 39
Dolag, K., Borgani, S., Murante, G., & Springel, V. 2009, MNRAS, 399, 497
Ford, A. B., Davé, R., Oppenheimer, B. D., et al. 2014, MNRAS, 444, 1260
Förster Schreiber, N. M., Übler, H., Davies, R. L., et al. 2019, ApJ, 875, 21
Garnett, D. R. 2002, ApJ, 581, 1019
Ginolfi, M., Jones, G. C., Béthermin, M., et al. 2020, A&A, 633, A90
Gonzalez-Jara, J., Tissera, P. B., Monachesi, A., et al. 2025, A&A, 693, A282
Hafen, Z., Faucher-Giguère, C.-A., Anglés-Alcázar, D., et al. 2019, MNRAS, 488, 1248
Hamel-Bravo, M. J., Fisher, D. B., Berg, D., et al. 2024, MNRAS, 530, 3855
Heckman, T. M., Alexandroff, R. M., Borthakur, S., Overzier, R., & Leitherer, C. 2015, ApJ, 809, 147
Herrera-Camus, R., Förster Schreiber, N., Genzel, R., et al. 2021, A&A, 649, A31
Hopkins, P. F., Quataert, E., & Murray, N. 2012, MNRAS, 421, 3522
Iwamoto, K., Brachwitz, F., Nomoto, K., et al. 1999, ApJS, 125, 439
Jiménez, N., Tissera, P. B., & Matteucci, F. 2015, ApJ, 810, 137
Kanehisa, K. J., Pawlowski, M. S., Heesters, N., & Müller, O. 2024, A&A, 686, A280
Katz, N., Hernquist, L., & Weinberg, D. H. 1999, ApJ, 523, 463
Kim, C.-G., Ostriker, E. C., Somerville, R. S., et al. 2020, ApJ, 900, 61
Knollmann, S. R., & Knebe, A. 2009, ApJS, 182, 608
Kohandel, M., Pallottini, A., & Ferrara, A. 2025, A&A, 704, A39
Krumholz, M. R., Kruijssen, J. M. D., & Crocker, R. M. 2017, MNRAS, 466, 1213
Lambas, D. G., Tissera, P. B., Alonso, M. S., & Coldwell, G. 2003, MNRAS, 346, 1189
Lapi, A., Salucci, P., & Danese, L. 2018, ApJ, 859, 2
Lee, H., Skillman, E. D., Cannon, J. M., et al. 2006, ApJ, 647, 970
Lelli, F., McGaugh, S. S., Schombert, J. M., Desmond, H., & Katz, H. 2019, MNRAS, 484, 3267
Llerena, M., Amorín, R., Pentericci, L., et al. 2023, A&A, 676, A53
Lodders, K. 2019, arXiv e-prints [arXiv:1912.00844]
Ma, X., Hopkins, P. F., Faucher-Giguère, C.-A., et al. 2016, MNRAS, 456, 2140
Maiolino, R., & Mannucci, F. 2019, A&A Rev, 27, 3
Martin, C. L. 1999, ApJ, 513, 156
McQuinn, K. B. W., van Zee, L., & Skillman, E. D. 2019, ApJ, 886, 74
McQuinn, K. B. W., Adams, E. A. K., Cannon, J. M., et al. 2022, ApJ, 940, 8
Mina, M., Shen, S., Keller, B. W., et al. 2021, A&A, 655, A22
Mishra, N., Johnson, S. D., Rudie, G. C., et al. 2024, ApJ, 976, 149
Mosconi, M. B., Tissera, P. B., Lambas, D. G., & Cora, S. A. 2001, MNRAS, 325, 34
Muratov, A. L., Kereš, D., Faucher-Giguère, C.-A., et al. 2015, MNRAS, 454, 2691
Muratov, A. L., Kereš, D., Faucher-Giguère, C.-A., et al. 2017, MNRAS, 468, 4170
Murray, N., Quataert, E., & Thompson, T. A. 2005, ApJ, 618, 569
Pandya, V., Fielding, D. B., Anglés-Alcázar, D., et al. 2021, MNRAS, 508, 2979
Peeples, M. S., Werk, J. K., Tumlinson, J., et al. 2014, ApJ, 786, 54
Péroux, C., & Howk, J. C. 2020, ARA&A, 58, 363
Perrotta, S., Coil, A. L., Rupke, D. S. N., et al. 2023, ApJ, 949, 9
Piacitelli, D. R., Brooks, A. M., Christensen, C., et al. 2025, ApJ, 993, 230
Pizzati, E., Ferrara, A., Pallottini, A., et al. 2023, MNRAS, 519, 4608
Planck Collaboration XVI. 2014, A&A, 571, A16
Raiteri, C. M., Villata, M., & Navarro, J. F. 1996, A&A, 315, 105
Roca-Fàbrega, S., Dekel, A., Faerman, Y., et al. 2019, MNRAS, 484, 3625
Roca-Fàbrega, S., Kim, J.-H., Hausammann, L., et al. 2021, ApJ, 917, 64
Rodríguez, S., Garcia Lambas, D., Padilla, N. D., et al. 2022, MNRAS, 514, 6157
Rosdahl, J., Schaye, J., Dubois, Y., Kimm, T., & Teyssier, R. 2017, MNRAS, 466, 11
Sales, L. V., Wetzel, A., & Fattahi, A. 2022, Nat. Astron., 6, 897
Scannapieco, C., Tissera, P. B., White, S. D. M., & Springel, V. 2005, MNRAS, 364, 552
Scannapieco, C., Tissera, P. B., White, S. D. M., & Springel, V. 2006, MNRAS, 371, 1125
Scannapieco, C., Tissera, P. B., White, S. D. M., & Springel, V. 2008, MNRAS, 389, 1137
Schroetter, I., Bouché, N., Wendt, M., et al. 2016, ApJ, 833, 39
Schroetter, I., Bouché, N. F., Zabl, J., et al. 2024, A&A, 687, A39
Somerville, R. S., & Davé, R. 2015, ARA&A, 53, 51
Springel, V. 2005, MNRAS, 364, 1105
Springel, V., White, S. D. M., Tormen, G., & Kauffmann, G. 2001, MNRAS, 328, 726
Sugahara, Y., Ouchi, M., Lin, L., et al. 2017, ApJ, 850, 51
Talbot, R. J., Jr, & Arnett, W. D. 1971, ApJ, 170, 409
Tinsley, B. M. 1980, Fund. Cosmic Phys., 5, 287
Tissera, P. B., Lambas, D. G., Mosconi, M. B., & Cora, S. 2001, ApJ, 557, 527
Tissera, P. B., White, S. D. M., & Scannapieco, C. 2012, MNRAS, 420, 255
Tissera, P. B., Bignone, L., Gonzalez-Jara, J., et al. 2025, A&A, 697, A134
Torrey, P., Cox, T. J., Kewley, L., & Hernquist, L. 2012, ApJ, 746, 108
Tremonti, C. A., Heckman, T. M., Kauffmann, G., et al. 2004, ApJ, 613, 898
Tully, R. B., & Fisher, J. R. 1977, A&A, 54, 661
Tumlinson, J., Peeples, M. S., & Werk, J. K. 2017, ARA&A, 55, 389
Vogelsberger, M., Genel, S., Sijacki, D., et al. 2013, MNRAS, 436, 3031
Weldon, A., Reddy, N. A., Coil, A. L., et al. 2024, MNRAS, 531, 4560
Woosley, S. E., & Weaver, T. A. 1995, ApJS, 101, 181
Zenocratti, L. J., De Rossi, M. E., Theuns, T., & Lara-López, M. A. 2022, MNRAS, 512, 6164

Appendix A: The Tully-Fisher relation

The CIELO galaxies follow the Tully-Fisher relation (TFR - Tully & Fisher 1977) as shown by Tissera et al. (2025). In this paper, we estimated it again, but for dwarf galaxies. The main goal is to estimate the potential well of the galaxies by using the rotational velocity as a proxy.

For this purpose, we obtained the rotational curves of the gas component for each galaxy and their progenitors by estimating the tangential velocity of each gas particle. The maximum rotational velocity, V_{max}, was measured as the mean tangential velocity within 0.5 kpc radial interval around the maximum value achieved. Additionally, we define the circular velocity, V_c, as the rotational velocity measured at R_{opt}. Both values are given in Table 1. When there is a well-defined gaseous disc in equilibrium within its potential well, we expect $V_c = \sqrt{GM_*/r}$. This is the case for the simulated galaxies with a disc. However, there are a few galaxies in which the gas components are not settled onto well-behaved discs, hence, the gas is more turbulent and dominated by dispersion. For these galaxies, we take V_c as the maximum value of the curve, V_{max}.

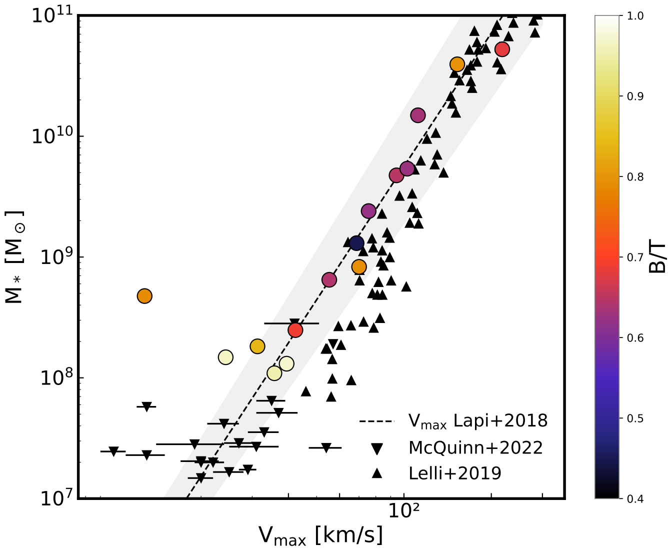

Fig. A.1. The Tully-Fisher relation obtained by using the maximum rotational velocity, V_{max}, for the CIELO galaxies, coloured by B/T. Observations by McQuinn et al. (2022, downwards-pointing black triangles) and Lelli et al. (2019, black triangles) are displayed from comparison. The best-fitting regression for the data of Lapi et al. (2018) is also shown (black, dashed line). The shaded region is defined by 1σ.

Figure A.1 displays the TFR for the simulated galaxies, coloured according to the B/T ratio. For comparison, the best-fitting linear regression (dashed line) $M_{bar} = 3.67 \times V_{max} + 2.41$ determined by Lapi et al. (2018) of local spiral galaxies was included. Additionally, we include observations of dwarf irregular galaxies by Lelli et al. (2019), where stellar masses were estimated by this author are based on 3.6 μm fluxes and velocities were measured at the peak of their rotational curves. Observational measurements of low-mass galaxies by McQuinn et al. (2022), which used rotational velocities estimated by using PV slices (position-velocity diagram) of HI zones are also included. Our CIELO galaxies follow the observed trend, except for very low-mass systems, which are mostly dominated by dispersion (0200, 2736, and 9110) and, hence, their V_{max} are smaller than expected, since we only estimated the TFR to have a characterisation of the simulated galaxies, calculating a correction to the TFR such as $S_{0.5}$ is beyond the scope of this paper (De Rossi et al. 2012).

Appendix B: The MZR for inflows

We present the MZR for the ISM (purple circles) and for the inflow around $z = 0$ (cyan circles) for our CIELO-P7 galaxies. Similar to Fig. 4, our simulated galaxies follow the MZR. We note that the inflows of these galaxies at $z = 0$ is mainly metal-poor gas, however, higher-mass galaxies tend to have slightly more enriched gas than sub-MW galaxies. As mentioned in Sect. 3, every galaxy has a unique SFH; therefore, sub-MW galaxies have a diversity in the inflow metallicity.

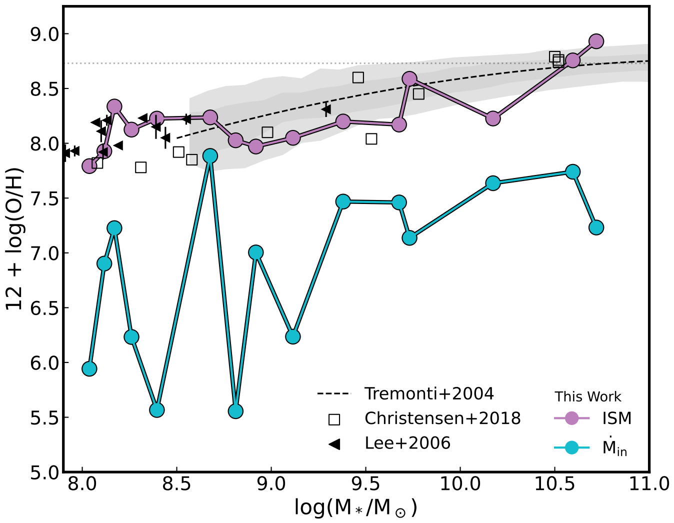

Fig. B.1. Mass-metallicity relation for the ISM (purple circles) and for the inflow rate around $z = 0$ (cyan circles). Symbols are described in Fig. 4.

Appendix C: Outflows for CIELO-P7 galaxies

Figure C.1 shows the unbound outflows, expelled mass rates, SFRs, and inflow rates as described in Sect. 3 for the remaining CIELO-P7 galaxies.

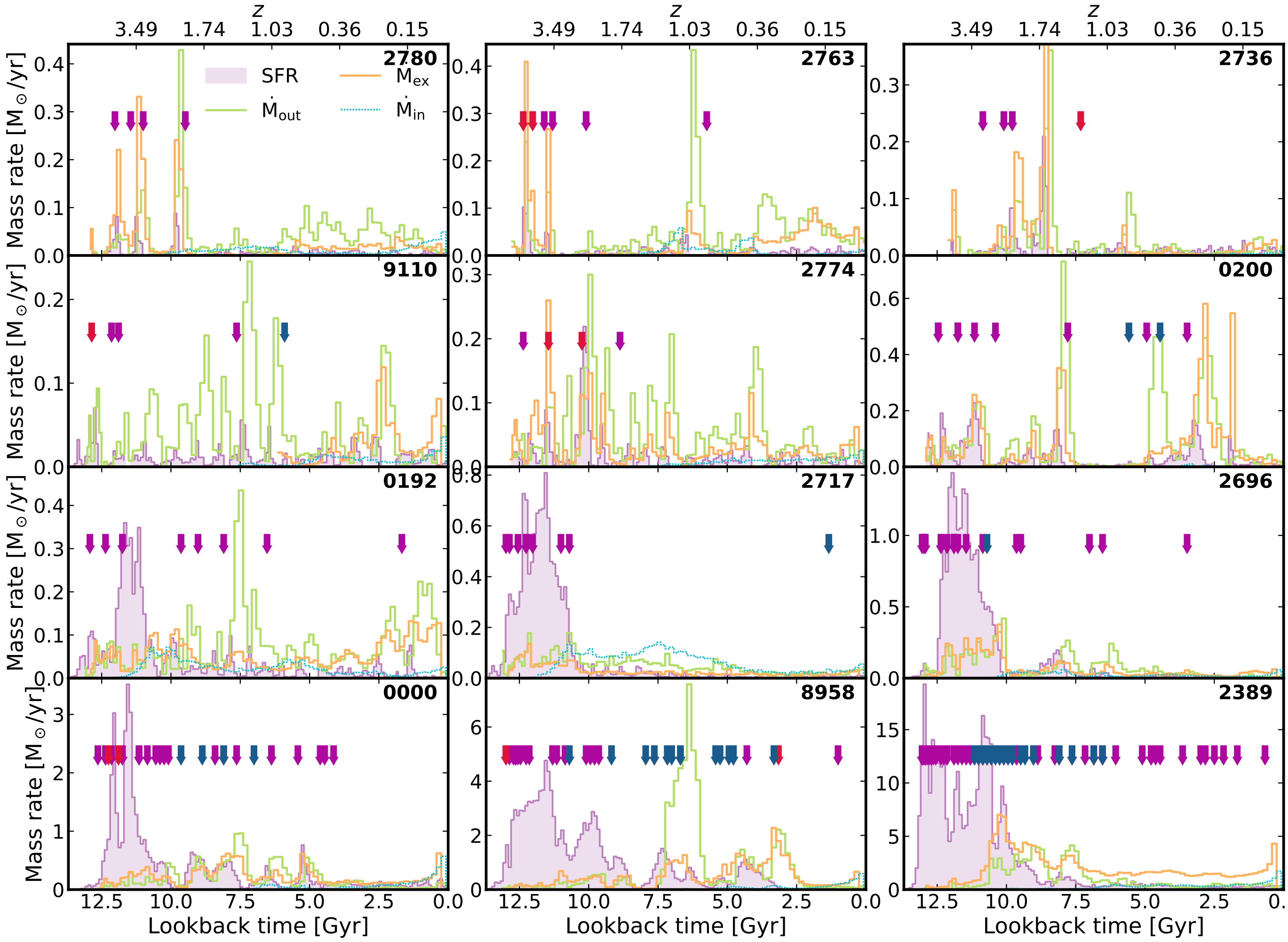

Fig. C.1. Evolution of SFR (purple shades), $\dot{M}_{out}$, the rate of unbound outflow for the inner shell [$1.5R_{opt}$, $0.5R_{200}$) (solid, green lines), $\dot{M}_{ex}$, the expelled mass rates (solid, orange lines), and $\dot{M}_{in}$, the inflow mass rate (dotted, cyan line) as a function of lookback time. The infall time of satellites (blue arrows) entering the virial radius, and the time of minor and major mergers (pink and red arrows, respectively) when corresponds.

Appendix D: Summary of main parameters.

Here we present a summary of the physical properties and main parameters obtained for our sample of CIELO-P7 galaxies summarised in Tables D.1, D.2, D.4 and D.3. In the case of D.3 we also provide the Spearman coefficients so the reader can use the fitted relations with caution depending on the level of statistical significance.

Table D.1. Physical properties of the selected CIELO galaxies at $z = 0$.

Galaxy ID	Σ_{gas} $M_\odot/pc^2$	Σ_* $M_\odot/pc^2$	$\log(T_{vir}/K)$	μ
2780	0.73	0.19	3.95	0.87
2763	0.54	0.24	4.09	0.80
2736	0.73	0.98	3.91	0.58
9110	0.51	0.57	3.97	0.68
2774	1.23	1.64	4.01	0.58
0200	0.31	2.60	4.16	0.26
0192	1.46	1.10	4.21	0.63
0181	1.78	0.53	4.25	0.77
2717	1.51	1.17	4.31	0.63
2696	1.10	3.93	4.48	0.34
2627	1.87	3.02	4.74	0.52
0000	1.91	9.75	4.69	0.34
8958	1.51	18.96	4.920	0.20
7805	0.76	41.63	5.32	0.28
2389	2.35	62.82	5.31	0.23

Notes. Columns from left to right summarise the gas surface density, stellar surface density, virial temperature, and gas fraction of the analysed galaxies.

Table D.2. Oxygen fraction per component for CIELO galaxies at $z = 0$.

Galaxy ID	$M_*/M_{O,gx}$	$M_g/M_{O,gx}$	$M_{ex}/M_{O,gx}$	$M_{in}/M_{O,gx}$	$M_H/M_{O,CGM}$	$M_W/M_{O,CGM}$	$M_L/M_{O,CGM}$	$M_C/M_{O,CGM}$
2780	0.15	0.85	0.17	0.06	0.00	0.00	0.68	0.31
2763	0.20	0.80	0.30	0.08	0.00	0.00	0.67	0.33
2736	0.31	0.69	0.20	0.02	0.00	0.00	0.71	0.29
9110	0.31	0.69	0.38	0.03	0.00	0.00	0.67	0.33
2774	0.45	0.55	0.36	0.03	0.00	0.01	0.80	0.19
0200	0.77	0.23	0.63	0.01	0.00	0.01	0.69	0.30
0192	0.79	0.31	0.15	0.04	0.00	0.01	0.76	0.23
0181	0.34	0.66	0.10	0.06	0.00	0.09	0.82	0.09
2717	0.73	0.27	0.04	0.01	0.00	0.01	0.82	0.17
2696	0.89	0.11	0.05	0.01	0.00	0.02	0.71	0.26
2627	0.73	0.27	0.13	0.03	0.10	0.05	0.70	0.17
0000	0.83	0.17	0.05	0.01	0.12	0.05	0.71	0.12
8958	0.96	0.04	0.06	0.00	0.06	0.05	0.73	0.17
7805	0.91	0.09	0.07	0.02	0.44	0.04	0.46	0.06
2389	0.93	0.07	0.04	0.01	0.67	0.02	0.29	0.02

Notes. Columns from left to right contain the oxygen fraction in the stellar component and the gas component of the galaxy's mass until $z = 0$, expelled and inflow oxygen fraction across $z = 0 - 7$ to the galaxy's total oxygen mass at $z = 0$, oxygen fraction of the CGM phase in forms of hot phase, warm ions, low ions, and cold phase.

Table D.3. Mass-loading factor measured in a redshift bin of $z \sim 0$, $z \sim 1$ and $z \sim 2$.

	$z \sim 0$			$z \sim 1$			$z \sim 2$		
Galaxy ID	$\eta^a_{\rm out}$	$\eta^b_{\rm out}$	$\eta_{\rm ex}$	$\eta^a_{\rm out}$	$\eta^b_{\rm out}$	$\eta_{\rm ex}$	$\eta^a_{\rm out}$	$\eta^b_{\rm out}$	$\eta_{\rm ex}$
2780	6.04	6.02	2.30	3.33	3.25	0.50	2.61	1.91	3.04
2763	4.32	4.32	2.78	3.86	3.65	0.99	1.83	1.71	0.16
2736	0.67	0.67	0.57	1.83	1.84	1.98	0.62	0.84	1.24
9110	1.65	1.64	1.53	4.00	3.41	0.11	2.90	2.66	0.00
2774	2.55	2.52	1.67	2.96	2.59	1.23	1.27	1.25	0.65
0200	2.92	2.91	2.43	2.62	2.58	1.42	1.33	1.24	0.91
0192	3.76	3.81	3.09	2.72	2.65	0.99	0.29	0.34	0.50
0181	2.01	2.02	0.94	1.22	1.53	0.49	0.59	0.93	0.47
2717	3.09	2.88	2.10	2.29	2.23	0.82	0.36	0.34	0.17
2696	2.58	2.29	3.10	1.27	1.18	0.73	0.32	0.29	0.30
2627	1.73	1.72	2.44	0.66	0.64	0.60	0.25	0.25	0.16
0000	0.66	0.68	0.99	0.88	0.78	0.75	0.27	0.24	0.29
8958	1.70	1.77	1.98	1.55	1.61	0.44	0.10	0.08	0.14
7805	3.73	3.83	5.72	1.19	1.11	1.45	0.07	0.05	0.10
2389	0.81	1.06	3.34	1.44	1.28	1.83	0.13	0.09	0.29

Notes. $\eta_{\rm out}$ are mass-loading factors for the unbound outflows measured in a radial bin ^{a}: [1.5R$_{\rm opt}$,0.5R$_{200}$) and ^{b}: [0.5R$_{200}$,R$_{200}$). $\eta_{\rm ex}$ are mass-loading factors for the expelled mass rate.

Table D.4. Best fitting parameters for the mass-loading factors.

		V$_{\rm c}$					M$_*$				
		η_{100}	β	$\sigma_{\eta_{100}}$	σ_β	r	η_*	β	σ_{η_*}	σ_β	r
$z \leq 0.5$	$\eta^a_{\rm out}$	2.26	0.30	0.45	0.27	-0.24 (0.390)	3.22	0.11	0.63	0.08	-0.28 (0.315)
	$\eta^b_{\rm out}$	2.28	0.28	0.46	0.27	-0.20 (0.475)	3.17	0.10	0.62	0.08	-0.24 (0.398)
	$\eta_{\rm ex}$	2.62	-0.46	0.30	0.19	0.47 (0.079)	1.57	-0.15	0.36	0.05	0.44 (0.104)
$z \sim 1$	$\eta^a_{\rm out}$	1.61	0.48	0.27	0.16	-0.66 (0.007)	2.92	0.21	0.23	0.05	-0.79 (0.001)
	$\eta^b_{\rm out}$	1.55	0.47	0.24	0.14	-0.68 (0.005)	2.76	0.20	0.20	0.04	-0.83 (0.000)
	$\eta_{\rm ex}$	0.99	-0.09	0.16	0.20	-0.09 (0.761)	0.83	-0.07	0.19	0.07	0.11 (0.694)
$z \sim 2$	$\eta^a_{\rm out}$	0.50	0.77	0.23	0.33	-0.84 (0.001)	1.09	0.30	0.21	0.11	-0.89 (0.001)
	$\eta^b_{\rm out}$	0.47	0.76	0.19	0.28	-0.90 (0.001)	1.03	0.29	0.16	0.09	-0.89 (0.001)
	$\eta_{\rm ex}$	0.64	0.38	0.25	0.49	-0.35 (0.206)	0.64	0.37	0.23	0.21	-0.47 (0.079)

Notes. $\eta = \eta_{100}({\rm V_c}/100{\rm kms^{-1}})^{-\beta}$ and $\eta = \eta_*({\rm M_*}/10^8{\rm M_\odot})^{-\beta}$ for the expelled mass ($\eta_{\rm ex}$), and for the unbound outflows measured in a radial bin ^{a}: [1.5R$_{\rm opt}$,0.5R$_{\rm R_{200}}$) and ^{b}: [0.5R$_{200}$,R$_{200}$). Columns from left to right contain $\eta_{100}(\eta_*)$, β, standard deviations $\sigma_{\eta_{100}}(\sigma_{\eta_*})$, σ_β, and the Spearman coefficients r and p (within parenthesis).